Experimental characterization of granular sodium borohydride under varying operational conditions across flow regimes

van Benten, M.C.; Padding, J.T.; Schott, D.L.

DOI
10.1016/j.powtec.2025.121739

Publication date
2025

Document Version
Final published version

Published in
Powder Technology

Powder Technology 469 (2026) 121739

Contents lists available at ScienceDirect

Powder Technology

journal homepage: www.journals.elsevier.com/powder-technology

Experimental characterization of granular sodium borohydride under varying operational conditions across flow regimes

M.C. van Benten [a],*, J.T. Padding [b], D.L. Schott [a]

[a] Maritime and Transport Technology, Delft University of Technology, Mekelweg 2, 2628CD, Delft, The Netherlands
[b] Process and Energy, Delft University of Technology, Leeghwaterstraat 39, 2628CD, Delft, The Netherlands

HIGHLIGHTS

- Dry $NaBH_4$ is free-flowing, but is affected by moisture and time consolidation.
- Time consolidation increases cohesion and reduces the flowability of $NaBH_4$.
- The effects of time consolidation on $NaBH_4$ are reversible with minimal agitation.
- Elevated moisture content accelerates time consolidation effects.
- The impact of moisture on the flowability of $NaBH_4$ is stronger for smaller particles.

GRAPHICAL ABSTRACT

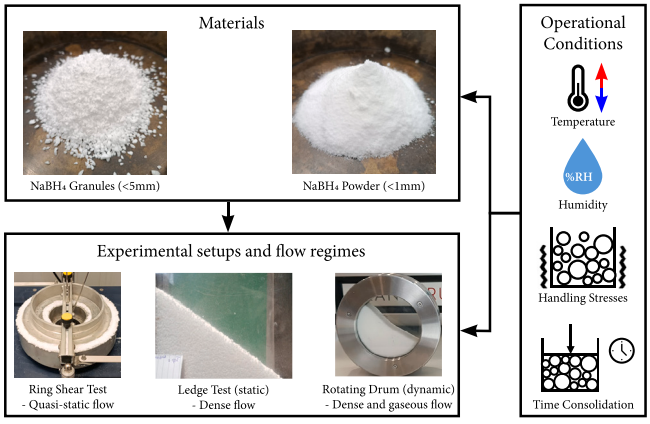

ARTICLE INFO

Keywords:
Sodium borohydride
Experiments
Mechanical characteristics
Flowability
Operational conditions
Flow regimes
Bunkering equipment

ABSTRACT

Sodium borohydride ($NaBH_4$) is increasingly considered as an alternative fuel for maritime vessels due to its relatively high energy density. When stored in dry solid form, it is a granular material, similar to coal, starch, and iron ore. As $NaBH_4$ is historically used in the chemical industry in aqueous solutions, virtually no details regarding its behaviour as a solid granular material are known. Therefore, after determining particle properties such as size, shape, and density, this study characterises granular $NaBH_4$ in three flow regimes using three experimental setups. Ring shear tests are used for the quasi-static regime, ledge tests for the dense flow regime, and rotating drum tests characterise both dense and gaseous flow, depending on the rotational speed. Various operational conditions, including temperature, humidity, time consolidation, and handling stresses, are taken into account. Experimental results demonstrate that above a threshold temperature and humidity, $NaBH_4$ readily absorbs moisture from ambient air but remains free-flowing for most scenarios. However, time consolidation can transform this free-flowing material into a very cohesive substance. While this cohesiveness is reversible, requiring minimal agitation, the transformation from free-flowing to cohesive is accelerated by elevated moisture contents and a reduced particle size. Additionally, handling stresses were found to have minimal effect on the flow behaviour and characteristics of $NaBH_4$. These findings are ultimately used to derive implications for the design of handling and storage equipment for $NaBH_4$, enabling its use as an alternative fuel for maritime vessels.

* Corresponding author.
E-mail address: m.c.vanbenten@tudelft.nl (M.C. van Benten).

https://doi.org/10.1016/j.powtec.2025.121739
Received 25 June 2025; Received in revised form 3 October 2025; Accepted 7 October 2025
Available online 17 October 2025

1. Introduction

Hydrogen is increasingly considered as an alternative fuel to reduce global emissions and battle climate change [1]. However, next to being the most abundant material in the universe, it is also the lightest, giving hydrogen a very low gravimetric energy density. This can be slightly improved by pressurising hydrogen to 700 bar or cooling it to −253 °C, both requiring thick-walled storage tanks to withstand the pressure or provide thermal insulation [2]. A more promising solution in terms of energy efficiency is to store hydrogen in carrier materials, such as sodium borohydride ($NaBH_4$), a so-called solid hydrogen carrier [3]. $NaBH_4$ is a granular bulk material, such as salt, sand, or iron ore, that has a higher energy density than pressurised or liquefied hydrogen, while at the same time it can be stored under ambient conditions. Many studies have already shown its potential [4–13], but using $NaBH_4$ as a fuel still presents challenges [14,15]. For example, because sodium borohydride is a granular material, its flow behaviour differs substantially from that of any conventional liquid or gaseous fuel. Compared to fluids, granular materials have effective internal friction and often cohesion between the individual grains, so the design of handling and storage equipment – e.g., silos, screw conveyors, and pneumatic conveying systems – for granular materials requires a thorough understanding of the material's behaviour first. Neglecting this could result in malfunctioning equipment, leading to, e.g. delays in vessel and port operations. In our previous study [16], we discussed the various properties of $NaBH_4$ relevant to equipment design that define the flow behaviour, referred to as mechanical characteristics, and highlighted that virtually none of these characteristics are reported in literature.

These mechanical characteristics can be measured. However, it is essential to recognise that they are not constant but depend on the prevailing flow regime [17–20]. Three flow regimes are typically distinguished. First, a quasi-static regime is defined, characterised by low flow velocity, where inertia forces of the individual grains can be neglected and the confining stresses dominate the behaviour. Second, a gaseous regime can be defined for high velocities. Here, the flow resembles the behaviour of a gas; grains are far apart and kinetic energy is high, and therefore inertia forces dominate the behaviour. Third, in between these regimes is a dense flow regime, where neither inertia nor confining stresses dominate the flow. The flow regime relevant for an application can be identified using the inertial number I, the ratio of inertia forces to confining stresses, and can be defined for confined and free surface flow as follows [20]:

$$I = \frac{\dot{\gamma} d}{\sqrt{\sigma/\rho}} \qquad \text{For confined flow} \qquad (1)$$

$$I = \frac{5}{2}\frac{\bar{V} d}{h\sqrt{ghcos(\theta)}} \qquad \text{For free surface flow} \qquad (2)$$

where $\dot{\gamma}$ is the shear rate [1/s], d the particle diameter [m], σ the normal stress [Pa], ρ the bulk density [kg/m^3], $\bar{V}$ the mean velocity [m/s], h the layer thickness [m], and θ the inclination of the flow [deg]. Using I, the three flow regimes can be described as follows [17,20–22]:

- Quasi-static regime: $I < (10^{-3} - 10^{-2})$
- Dense flow regime: $(10^{-3} - 10^{-2}) < I < (0.1 - 0.3)$
- Gaseous flow regime: $I > (0.1 - 0.3)$

Note that the regimes are not sharply defined due to the mechanical characteristic known as the coefficient of restitution (e). For higher coefficients of restitution, granular flows transition to another regime at lower I [20]. Additionally, the surface friction affects the collision mechanisms (frictionless, sliding, or rolling), mainly within the dense flow regime [23–25]. For illustration purposes, the flow regime boundaries are shown as a function of stress and particle diameter for different values of the coefficient of restitution in Fig. 1.

Typically, gaseous flow is observed at a silo inlet, while the flow inside the silo and the discharge flow of the hopper can be characterised as quasi-static or dense flow, depending on i.e. the dimensions of the equipment [26–28]. Flow in screw conveyors is quasi-static or dense, depending on the rotational speed [29], and flow in pneumatic conveyors can be either dense or gaseous [30]. Consequently, any design of handling and storage equipment requires knowledge of the flow behaviour and mechanical characteristics of $NaBH_4$ in and across the flow regimes. Even more, next to the flow regime, operational conditions such as the temperature and relative humidity of the ambient air, handling (repeated stress impact), and time consolidation (compression for an extended period) can significantly alter the mechanical characteristics and lead to e.g., changes in cohesion, internal friction, wall friction, and flowability [31–38], and should therefore be taken into account when characterising granular materials.

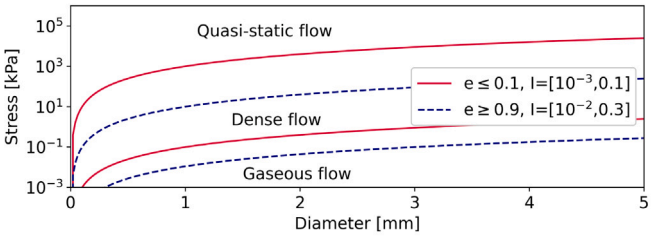

Fig. 1. Flow regime as a function of stress and particle diameter.

Fig. 2. Samples of the $NaBH_4$ used for this study with (a) granules and (b) powder.

To the best of our knowledge, this is the first comprehensive study to investigate the mechanical characteristics of $NaBH_4$ across distinct flow regimes while also examining the influence of varying operational conditions relevant to handling and storage equipment design. To this end, we first describe the material properties of $NaBH_4$. Next, we provide an overview of the experimental setups and how these are used to identify the effect of varying operational conditions and the different flow regimes. We then present the result of the experiments and conclude with the implications of these findings on handling and storage equipment for the bunkering of $NaBH_4$.

2. Materials and methods

2.1. Materials

The materials used for this study are $NaBH_4$ granules (< 5 mm) and powder (< 1 mm), shown in Figs. 2(a) and 2(b), respectively. Both have a reported purity of 98% or higher, with a moisture content below 0.3%, and a molecular weight of 37.83 g/mol [39].

2.2. Material properties

To determine the particle size of the $NaBH_4$, both sieving analysis and laser diffraction are used, and the $NaBH_4$ was sampled before and

Table 1
Particle shape analysis (number) of $NaBH_4$ granules and powder with imaging (2D).

Sample	Property	D10	D50	D90	Mean	Span
Granules 964 particles	Circularity	0,808	0,858	0,897	0,855	0,104
	Convexity	0,911	0,938	0,956	0,936	0,048
	Aspect Ratio	0,559	0,728	0,896	0,724	0,463
	Width	1.75 mm	2.57 mm	3.50 mm	2.60 mm	0.530
	Length	2.57 mm	3.52 mm	4.64 mm	3.58 mm	0.434
Powder 9749 particles	Circularity	0,824	0,906	0,954	0,898	0,143
	Convexity	0,933	0,975	0,992	0,972	0,061
	Aspect Ratio	0,512	0,736	0,902	0,722	0,530
	Width	162 μm	267 μm	366 μm	270 μm	0.610
	Length	202 μm	337 μm	476 μm	340 μm	0.686

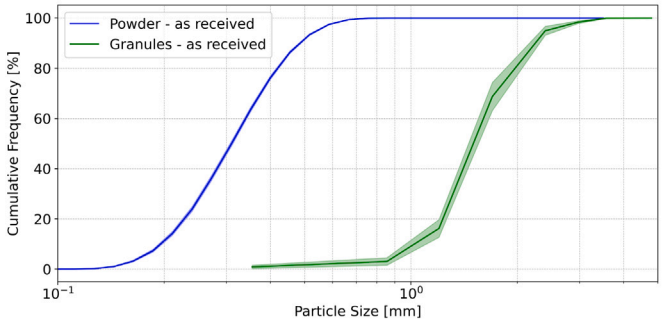

Fig. 3. Particle size distributions (mass) of $NaBH_4$ granules (N = 5) and powder (N = 25) as received from CPH Chemicals. Coloured bands represent the 95% confidence interval.

after experiments. Sieve analysis proved well suited for the granules, but the powder showed too much cohesion and adhesion for the equipment to reliably measure the particle size distribution (PSD) in this manner. Hence, laser diffraction is used to determine the PSD of the powder samples. The particle shape was analysed with imaging to provide a 2D shape representation of the $NaBH_4$ samples. The particle density analysis was determined using gas pycnometry with helium.

Particle Size: Sieve Analysis and Laser Diffraction

For the granules, sieve analysis is carried out following the ASTM C136/C136M-19 Standard Method for Sieve Analysis of Fine and Coarse Aggregates, using the Haver & Boecker Test Sieve Shaker. A stack of 7 sieves with the following (square) mesh sizes was used: 4.0 mm, 3.2 mm, 2.8 mm, 2.0 mm, 1.4 mm, 1.0 mm, and 0.71 mm. For each measurement, 200 g of material is charged in the top (4.0 mm) sieve. Each sample is sieved for 9 min with 15-second intervals and an amplitude of 1 mm. After 9 min, the remaining $NaBH_4$ on each sieve is weighed with a scale (Kern EMS 12K0.1), and as such, a particle size distribution can be obtained for each sample. In total, 5 samples are sieved, and the resulting PSD can be seen in Fig. 3.

For the powder samples, laser diffraction measurements were performed with the Malvern Mastersizer 3000. Because the maximum sample size per test is limited (approx. 5 g), five powder samples are taken for each granule sample of the sieve analysis, totalling 25 powder samples. Each sample is drawn through the device, past the lasers, with an air pressure of 2 bar. The feed rate was manually adjusted such that the flow is sufficiently slow to make accurate measurements (incorrect measurements will be indicated by the software). The mean particle size distribution with the 95% confidence interval of the 25 samples is shown in Fig. 3.

Particle Shape: Imaging

Imaging was used to obtain information regarding the shape of $NaBH_4$ powder and granules. The analysis was carried out with the Malvern Morphology G3SE with a Nikon CFI Brightfield/Darkfield inspection microscope (Eclips L200ND) and a Baumer 5 M pixels CCD digital colour camera. Due to the difference in size, samples of $NaBH_4$ granules and powder were prepared and processed slightly differently. Granules were manually dispersed on an object glass, and due to the rather large particles, a magnification of 2.5x is sufficient. To achieve an accurate focus across the entire body of small and large three-dimensional particles, up to 4 images at different focal points are taken of a particle and then merged to provide a single composed image. As the powder particles are much smaller, samples (19 mm^3) were dry dispersed in air with the aid of the Solid Dispersion Unit (SDU) on an object glass with the following settings: an air pulse of 1 bar during 20 ms and a settling time of 600 s. Due to the (rather) narrow particle size distribution and small particles, a magnification of 5x is used. To achieve an accurate focus across the entire body of small and large three-dimensional particles, up to 6 images at different focal points are taken of a particle and then merged to provide a single composed image. During the analysis for both samples, a gas flow of nitrogen was blown over the samples to minimise moisture uptake, as otherwise only droplets were present on the object glass after the measurement. The circularity, convexity, aspect ratio, width, and length of the particles are presented in Table 1. D10, D50, and D90 denote the particle diameters at which 10%, 50%, and 90% of the sample's cumulative distribution is reached, respectively. The span, calculated as (D90-D10)/D50, is a measure of the width of the PSD. Note that the imaging results are based on the number of particles, not mass, and provide a 2D representation of the particles. Therefore, a high circularity does not mean a high sphericity, and also, the convexity might be different if a 3D view of the particles is considered.

Table 2
Skeletal density of $NaBH_4$ samples with 95% confidence interval.

Skeletal Density of $NaBH_4$ [g/cm^3]	Measurements (sample size: 39–45 g)			Mean	95%CI
Granules	1.045	1.046	1.051	1.047	[1.039–1.056]
Powder	1.077	1.077	1.078	1.077	[1.076–1.079]

Particle Density: Gas Pycnometry

The particle density of the $NaBH_4$ powder and granules is determined using gas pycnometry with helium. The experiments are carried out with the Anton Paar Ultrapycnometer 5000 at a temperature of 25 °C, in accordance with standard ISO 12154:2014.1. Three samples of 39 g - 45 g each were used to analyse the $NaBH_4$ granules and powder, and the results of the analysis are shown in Table 2.

Moisture Analysis

The purchased $NaBH_4$ is reported to contain up to 0.3% moisture, and for both granules and powder, this is verified according to the ASTM *Standard Test Method for Total Evaporable Moisture Content of Aggregate by Drying*. The moisture absorption characteristics of the purchased $NaBH_4$ samples were not provided by the supplier and will therefore be investigated in the method section.

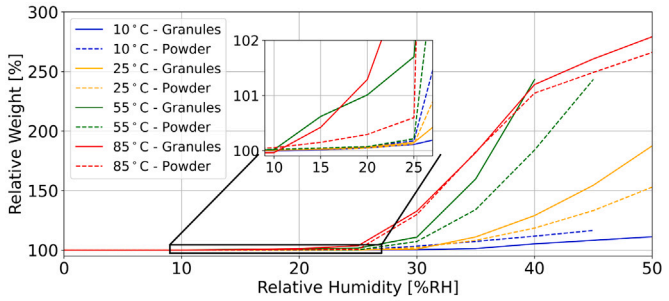

Fig. 4. Hygroscopic behaviour of $NaBH_4$ granules (31–66 mg) and powder (40–64 mg). Accuracy of the humidity sensor is ±1 RH%. Relative humidity levels are kept constant for 90 min and increased in steps of 5%. Each combination of temperature and sample size is executed once (N = 1). The microbalance has a resolution of 1 μg, and a baseline drift of 1 μg per week.

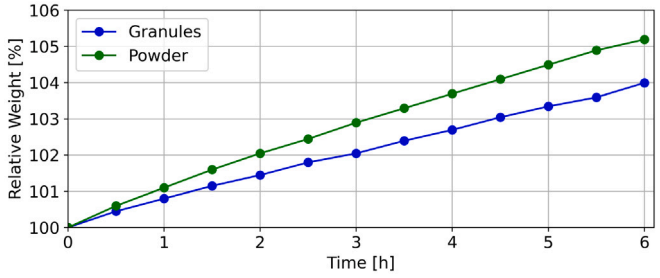

Fig. 5. Moisture absorption of $NaBH_4$ granules (200.3 g) and powder (200.3 g). T = 20–21 °C, RH = 65%–70%. N = 1.

2.3. Methods

In the experiments presented in this study, $NaBH_4$ is often exposed to ambient air. Due to its hygroscopic nature [40] it can absorb moisture from the air, effectively changing the sample during experiments. While sufficiently dry air (< 19% RH) prevents moisture uptake [41], the critical humidity threshold is temperature-dependent [42], and, to the best of the authors' knowledge, it is still unknown whether material properties such as particle size affect this. To this end, Dynamic Vapour Sorption experiments with the IGAsorp Dynamic Vapour Sorption (DVS) Analyser are conducted. The primary goal of this experiment is to identify a range of RH levels at which $NaBH_4$ starts to absorb moisture, and how this onset is affected by temperature. Samples of $NaBH_4$ (31–66 mg) are exposed to a flow of nitrogen gas (250 ml/min) with a predefined relative humidity. The relative humidity is increased in steps of 5% and held for 90 min. This allows for observing moisture absorption behaviour without the need to reach equilibrium at each step. This procedure is repeated using multiple temperature settings, effectively quantifying the combined effect of temperature and relative humidity on moisture absorption onset of the $NaBH_4$ samples.

Fig. 4 illustrates the relation between temperature, humidity, and particle size on the hygroscopic behaviour (more elaborate data of the DVS tests can be found here [dataset] [43]). The IGAsorp DVS Analyser has an accuracy of 1% RH. Although the measurements were not repeated, the data clearly shows that, except at 10 °C, the granules absorb more moisture than the powder at the same humidity level. Furthermore, the threshold for moisture absorption is temperature-dependent: no significant moisture uptake occurs below 10 ± 1% RH, and only minimal moisture absorption is observed at higher temperatures within the range of 10 ± 1%<RH< 25 ± 1%. Above 25 ± 1% RH, moisture absorption appears consistent for each humidity level, suggesting that equilibrium has not yet been reached. Additionally, for

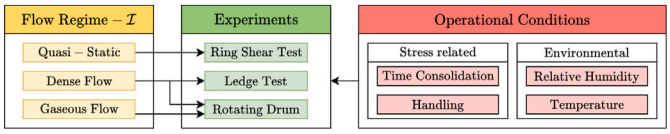

Fig. 6. Methodology for experimental characterisation of $NaBH_4$.

all temperatures except 85 °C, the moisture absorption rate continues to increase with increasing humidity, while at 85 °C it appears to decline at the highest humidity levels. However, the sample size of the DVS test is relatively small. To gain further insights into the moisture absorption behaviour on a laboratory scale, approximately 200 g of both granules and powder were exposed to ambient air (RH > 26%) for 6 h, and the weight was measured every 30 min. The results are shown in Fig. 5, and we can conclude that both granules and powder absorbed moisture at a slow, steady rate, with powder consistently absorbing more than granules. The results indicate no signs of saturation. After 6 h, visible caking was observed on the powder surface, while granules appeared largely unaffected.

Methodology

In the remainder of this section, the experimental setups that are used to characterise the flow behaviour of $NaBH_4$ are discussed. First, ring shear tests (Schulze Ring Shear Tester RST-01.pc) characterise the behaviour of $NaBH_4$ in the quasi-static regime. Second, the ledge test is used to determine the behaviour in the dense flow regime, and a rotating drum (GranuDrum) is used to characterise both the dense flow and the gaseous flow regime. Next to this, the effect of relevant operational conditions – temperature, relative humidity, handling stresses, and time consolidation stresses – expected for handling and storage equipment are also taken into account, schematically shown in Fig. 6. Note that the stress-related conditions – handling and time consolidation – are physical, meaning that the grains are repeatedly and/or for an extended period of time compressed and decompressed. We compare exposed and non-exposed samples, and from the difference in response, we can derive the effect on flow behaviour. Environmental conditions, on the other hand, act through a medium, in most cases, air. Similar to the stress-related conditions, we compare the response of samples exposed to different environmental conditions to derive their effects. It is important to note that we do not directly observe the effect of relative humidity. Instead, we test the effect of moisture content in the samples, which is affected by relative humidity. By accounting for moisture content, we can better understand the impact of relative humidity on the samples.

Ring Shear Tests

Ring shear tests are used to characterise $NaBH_4$ in the quasi-static flow regime, and experiments are performed with the Schulze Ring Shear Tester (Fig. 8(a) [44]), according to ASTM Standard D-6773 – Standard Test Method for Bulk Solids Using Schulze Ring Shear Tester. The annular shear cell is manually filled with $NaBH_4$ (approximately 500–600 g), and the lid is placed on top. A weight (F_N) and counterweight (F_A) ensure that the lid presses on the sample with the desired normal stress. The cell rotates with angular velocity ω, shearing the sample. By measuring the force on the load beams (F_1 and F_2), the effective shear stress transferred by the sample is monitored. Individual yield loci are measured for granules using the preshears and normal stress levels shown in Table 3, with a new sample for each yield locus. For all experiments, the shear velocity $v = \omega r$ is set to 1.5 mm/min. Measurements for individual yield loci are repeated three times. Each yield locus is analysed to derive the following metrics, as shown in Fig. 7: effective internal friction (ϕ_e), cohesion (τ_c), unconfined yield strength σ_c, consolidation strength (σ_1), and flow function constant ($\mathrm{ff_c}$). The latter is defined as the ratio of the consolidation stress to the unconfined yield strength: $\mathrm{ff_c} = \sigma_1/\sigma_c$, and is used to classify the flow

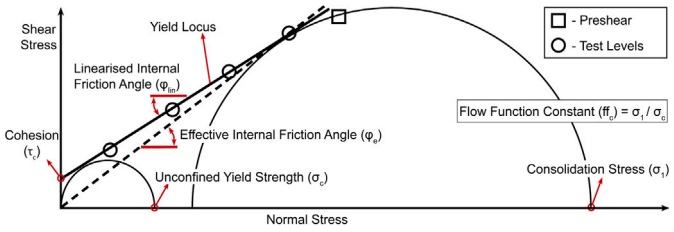

Fig. 7. Yield loci analysis.

Table 3
Individual ring shear test stress levels. Colours highlight similar stress levels.

Preshear [kPa]	Normal Stress Levels [kPa]			
20	4,0	6,4	11,2	16
16	3,2	6,4	9,6	12,8
12	2,4	4,8	7,2	9,6
8	1,6	3,2	4,8	6,4
4	0,8	1,6	2,4	3,2
2	0,4	0,8	1,2	1,6
1	0,2	0,4	0,6	0,8

Table 4
Flowability according to the flow function constant (ff_c) [45].

Flow function constant	ff_c
Not flowing	<1
Very cohesive	$1 \leq ff_c < 2$
Cohesive	$2 \leq ff_c < 4$
Easy-flowing	$4 \leq ff_c < 10$
Free-flowing	≥ 10

Table 5
Sequential ring shear test stress levels. Colours highlight similar stress levels.

Preshear [kPa]	Normal Stress Levels [kPa]				
20	1,0	1,6	6,4	11,2	16
16	0,8	3,2	6,4	9,6	12,8
12	0,6	2,4	4,8	7,2	9,6
8	0,4	1,6	3,2	4,8	6,4
4	0,2	0,8	1,6	2,4	3,2
2	0,1	0,4	0,8	1,2	1,6
1	0,05	0,2	0,4	0,6	0,8

Table 6
Wall ring shear test stress levels.

	Normal stress levels									
#	1	2	3	4	5	6	7	8	9	10
kPa	1	2	3	4	6	8	10	12	16	20

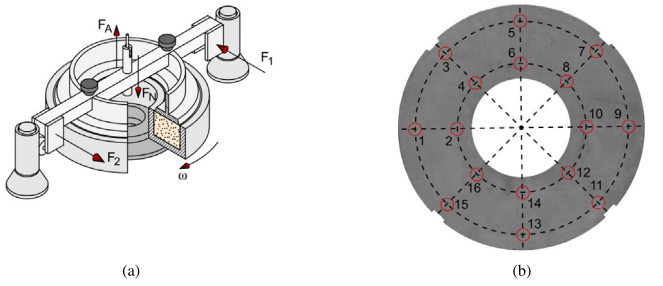

Fig. 8. Schematics of a ring shear tester [44] (a) and stainless steel wall sample measurements (b).

behaviour into different regimes – from free-flowing to not flowing – according to Table 4. The bulk density (ρ_b) of the samples is derived using the vertical displacement of the shear cell lid. Ambient conditions during the experiments – 20–25 °C and 30%–50% RH – are assumed to have minimal on the samples during experiments, which is confirmed in Section 3.6.

Effect of Handling

The effect of handling on $NaBH_4$ samples for confined flow – attrition or breakage – due to repetitive shearing under pressure is determined using sequential ring shear tests. These yield loci are measured using the same stress levels as the individual ring shear tests, with an additional normal stress level, as shown in Table 5. The key difference is that the same sample of powder and granules is used for all yield loci, from low to high preshear levels, simulating cumulative mechanical stress during handling. Measurements for sequential yield loci are repeated five times, each repetition with a new sample. After testing, the particle size distribution is measured and compared to the 'as-received' particle size distributions, such that attrition or breakage can be identified. Furthermore, the sequential yield loci are compared with the individual yield loci to detect changes of effective internal friction, cohesion, flowability, and bulk density—characteristics that could be influenced by attrition or breakage.

Effect of Relative Humidity

To determine the effect of relative humidity, individual yield loci of $NaBH_4$ are measured for samples containing 2%, 4%, and 6% moisture for preshear stresses of 4 kPa, 8 kPa, and 16 kPa.

Wall Friction Tests

Where regular shear tests characterise bulk behaviour, wall friction tests can be used to characterise material-wall interactions, effectively measuring the friction and adhesion between the $NaBH_4$ and different wall samples. The wall friction is measured using the Schulze Ring Shear Tester with the wall shear cell, and the used normal stresses are shown in Table 6. A total of three wall materials are considered: perspex, stainless steel, and aluminium; each test is repeated five times. An example of a wall sample is shown in Fig. 8(b). The wall samples are cleaned with ethanol before testing, but not between repetitions.

Surface Roughness

The surface roughness of the wall samples is determined using the TESA-Rugosurf 20. Since a typical measurement captures only 1–5 mm of the surface, each wall sample is divided into eight sections. Within each section, roughness is measured at two points: 2 cm from both the inner and outer edges, as illustrated in Fig. 8(b). This approach results in 16 measurements per wall sample, ensuring a representative evaluation of surface roughness.

Time Consolidation Tests

The effects of time consolidation are investigated through shear tests with both the Schulze Ring Shear Tester and the Brooklyn Powder Flow Tester. The latter operates similarly to the Schulze Ring Shear Tester but has a smaller shear cell, requiring less $NaBH_4$ to fill (approximately 250–300 g). The procedure starts by measuring the (instantaneous) yield locus, similar to the procedure for the Schulze Ring Shear Tester. Based on this yield locus, the consolidation stress σ_1 is determined and applied to the sample for a specific period of time (t). Note that before the loading period, the sample is sheared under the preshear stress until steady-state flow is reached. After this consolidation period, the sample is loaded with the post-consolidation normal stress, sheared till failure, and the corresponding shear stress is noted. For each consolidation time and preshear level, a new sample is used, resulting in 24 samples (6 consolidation times and 4 preshear levels) for both powder and granules, and the applied stress levels and consolidation times are shown in Table 7. The tests are conducted in a climate chamber maintained at 20 °C and below 10% RH to prevent moisture uptake.

Table 7
Preshear and normal stress levels, consolidation stresses, consolidation times, and post-consolidation normal stress levels for time-consolidated shear tests with the Brooklyn powder flow tester. Colours highlight similar stress levels.

Preshear [kPa]	Normal Stress Levels [kPa]					Consolidation Stress [kPa]	Consolidation Times [h]	Post-Consolidation Normal Stress [kPa]
4.0	0.8	1.6	2.4	3.2	4.0	4.8[a]	[1, 2, 4, 8, 16, 24]	4.0
3.0	0.6	1.2	1.8	2.4	3.0	4.8[a]	[1, 2, 4, 8, 16, 24]	3.0
2.0	0.4	0.8	1.2	1.6	2.0	$\sigma_{1:2}$[b]	[1, 2, 4, 8, 16, 24]	2.0
1.0	0.2	0.4	0.6	0.8	1.0	$\sigma_{1:1}$[b]	[1, 2, 4, 8, 16, 24]	1.0

[a] Maximum normal stress that could be applied by the apparatus.
[b] Corresponding consolidation stress (σ_1) of the yield loci for 1 kPa ($\sigma_{1:1}$) and 2 kPa ($\sigma_{1:2}$) preshear.

Table 8
Preshear and normal stress, consolidation stress, consolidation times, post-consolidation normal stress, and repetitions for time-consolidated shear tests with the Schulze ring shear tester.

Preshear [kPa]	Normal stress [kPa]	Consolidation stress [kPa]	Consolidation times [h]	Post-consolidation normal stress [kPa]	Repetitions [#]
4.0	2.4	10.115	[8, 16, 32, 64, 128]	2.4	3[a]

[a] Only two repetitions were performed for the 32-hour and 64-hour consolidation times.

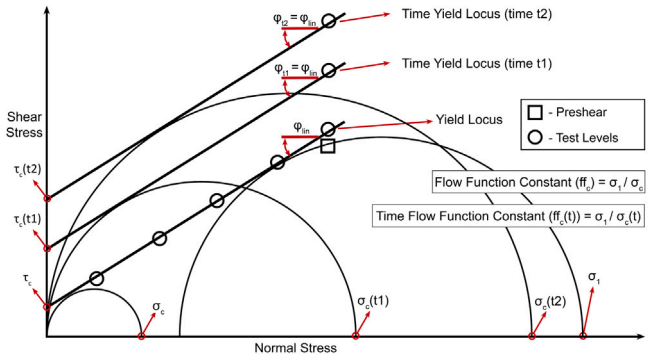

Fig. 9. Time yield loci analysis.

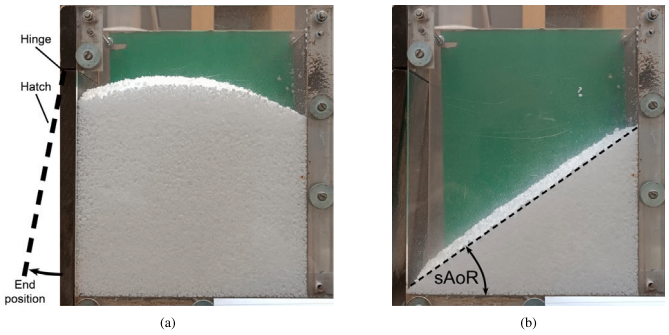

Fig. 10. Ledge test with $NaBH_4$ granules with (a) before opening of the hatch and (b) after opening of the hatch with visualised sAoR.

The analysis of the yield loci before the time consolidation periods (instantaneous yield loci) is similar to the approach shown in Fig. 7. For the time yield locus, a straight line is constructed with the same linearised friction angle as the instantaneous yield locus ($\phi_t = \phi_{lin}$), passing through the measured shear stress at the post-consolidation normal stress, as illustrated in Fig. 9. The intersection of the time yield locus with the shear stress axis determines the cohesion ($\tau_c(t)$), and the construction of an unconfined Mohr circle results in the unconfined yield strength ($\sigma_c(t)$). The flow function constant for the time yield locus is defined as: $\mathrm{ff}_c(t) = \sigma_1/\sigma_c(t)$.

For time consolidation tests with the Schulze Ring Shear Tester, the procedure was slightly different, as the instantaneous yield loci had already been measured during regular shear tests. After filling the shear cell, samples were sheared under the preshear stress until steady-state flow was reached and directly loaded with the consolidation stress σ_1. After the consolidation time had passed, the samples were sheared under the post-consolidation normal stress until failure. Contrary to the time consolidation tests with the Brooklyn Powder Flow Tester, multiple repetitions could be performed. The applied stress levels, consolidation times, and number of repetitions are shown in Table 8. No climate chamber was available, and ambient conditions fluctuated between 20–25 °C and 20%–45% RH. Due to the slight gap between the shear cell and the lid, moisture uptake could not be prevented. Therefore, samples used for 128-hour consolidation were analysed post-experiment for moisture content. Additionally, the particle size distribution was redetermined and compared to the as-received samples to detect possible breakage or attrition during long-term storage and subsequent handling.

Ledge Tests

The ledge test [46], also known as the shear box [47], or rectangular container test [48], is used to determine the static angle of repose (sAoR). The setup is shown in Fig. 10. The box is 250 mm high, 183 mm long, and has an adjustable width, here set to 100 mm. The container is manually filled with 1916.7 g (granules) or 1995.1 g (powder) of $NaBH_4$, slowly poured from the top of the box to minimise consolidation effects. Once the material has settled, the hatch is opened rapidly, allowing the sample to flow, resulting in a slope with a static angle of repose. The slope is recorded with a 108 MP camera. The images are edited to account for lens distortion, and all images are given a uniform green background. A MATLAB script [dataset] [43] is used to identify the slope of the material. Next, a straight line is fitted to this slope, and the angle of this fit is the static angle of repose (sAoR). The test is repeated 10 times with the same sample, both for the granules and for the powder. During the experiments, the samples were exposed to ambient conditions – 20–25 °C and 30%–40% RH – but we assume no significant amount of moisture was absorbed during the experiments, as the 10 repetitions took less than 15 min.

Effect of Relative Humidity and Temperature

To investigate how moisture and temperature affect the angle of repose of $NaBH_4$, a climate chamber was used. The chamber was set to a temperature of 60 °C and a humidity level of 25% RH. In this controlled environment, $NaBH_4$ gradually absorbed moisture. A sample of granules, previously used to obtain the data in Table 10, underwent conditioning three times in the climate chamber. Before and after each conditioning period, the sample is weighed to determine the amount

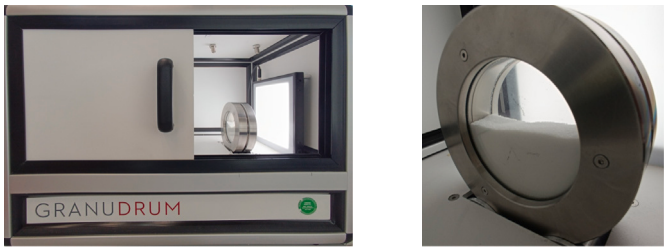

(a) (b)

Fig. 11. GranuDrum setup with (a) picture of the equipment and (b) close-up of $NaBH_4$ powder in the drum.

of absorbed moisture. Additionally, after each conditioning period, the ledge test was performed multiple times. As the ledge test was exposed to ambient conditions during testing, the sample gradually cooled down. To this end, before each repetition, the temperature of the sample was measured with a thermometer. The same procedure as previously discussed is used to record the slopes and obtain the sAoR.

Effect of Time Consolidation

The effect of time consolidation is determined by leaving the $NaBH_4$ to settle in the ledge box for 0.5, 1, and 2 h before proceeding with the measurements. Ambient conditions were above the moisture absorption limits, and therefore, the setup was covered with a lid to minimise moisture absorption.

Rotating Drum Tests

Fig. 11(a) shows the rotating drum setup used to characterise the dynamic angle of repose, together with a close-up of the rotating drum filled with $NaBH_4$ powder in Fig. 11(b). The experiments were conducted using the GranuDrum (provided by Granutools), which has a total volume of 110 mL, with a drum diameter of 84 mm and an axial length of 20 mm. The side walls of the drum are constructed from glass, allowing for optical measurements of the material flow. An LED panel ensures sufficient illumination of the drum, while a camera (a 5-megapixel monochrome CMOS camera) records images at the opposite end (gain of 10 and an exposure of 1.85 ms) as the drum rotates at varying rotational speeds. Due to the relatively small size of the GranuDrum, 5 samples of both granules and powder were taken from the $NaBH_4$ used for ring shear test experiments. The sample size was such that the drum had a fill ratio between 50% and 55%, a range commonly used for rotating drum experiments. Six speed settings were used: [1, 5, 10, 20, 40, 60] rpm, and images were captured at a frame rate of 5 frames per second over a total duration of 20 s per measurement. Ambient conditions – 20 °C and 20%–30% RH – during the experiments have minimal effect on the $NaBH_4$ as the samples are contained in the small, closed environment of the GranuDrum for the duration of the test.

Effect of Handling

To emulate the effect of repetitive stress impact (handling) on the $NaBH_4$ samples during free surface flow, the rotational speed of the drum was incrementally increased from 1 to 60 rpm and then decreased back to 1 rpm. The resulting hysteresis – the difference in dynamic angle of repose and the cohesive indices of increasing and decreasing rotational speed cycles – functions as an indicator for the material's sensitivity to these handling stresses.

Effect of Time Consolidation

To investigate the effect of time consolidation – specifically, the duration of the effects – on the $NaBH_4$, the samples were allowed to consolidate for both 5 and 10 min following the standard tests. After consolidation, the drum was slowly rotated at 1 rpm for 40 s. The frame rate, duration, gain, and exposure were kept constant. During the initial phase of rotation, the material bed remained static, with surface angles up to 90°, indicating high resistance to flow. As the software of the GranuDrum initiates data acquisition only upon first detection of material flow, supplementary video recordings ([dataset] [43]) were taken manually from standstill to the point at which the software began recording the flow, and snapshots are shown in Appendix C.

Table 9
Classification of flow using cohesive index [50].

Flowability	Cohesive index
Excellent	<5
Good	5 ≤ CI < 10
Fair	10 ≤ CI < 20
Passable	20 ≤ CI < 30
Poor	30 ≤ CI < 40
Very poor	40 ≤ CI < 50
Very, very poor	≥ 50

Dynamic Angle of Repose

Fig. 12 illustrates the analysis of the rotating drum (GranuDrum) results. For each material type (powder or granules), sample (1 to 5), rotational speed (1 to 60 rpm), and rotation sequence (increasing or decreasing speed), 100 frames were captured. The GranuDrum software automatically detects the material–air interface in each frame and fits a straight line, $y_{k,fit}$, to each interface $y_k(x)$, as shown in Fig. 12a. Additionally, (a part of) the average interface across all frames, $\overline{y}(x)$, is fitted with a linear line, y_{fit}. This approach is described in detail by Neveu et al. [49] and is illustrated in Fig. 12b.

Next to the default GranuDrum analysis, two alternative methods were employed to characterise the dynamic angle of repose (dAoR). First, a linear fit $\overline{y}_{lin.fit}(x)$ minimising the root-mean-squared-error (RMSE) was applied to the average interface $\overline{y}(x)$ (Fig. 12c). Second, a novel approach is introduced in which the average material–air interface is characterised by a piecewise linear fit $\overline{y}_{piecewise}(x)$, consisting of three linear segments, enabling a more detailed representation of the slope. This method is illustrated in Fig. 12d, and its formulation is provided in Eq. (3) in Box I.

The corresponding dynamic angle of repose (dAoR) is defined as the slope of the fitted line(s) in Fig. 12a-d. For the piecewise method, this results in three distinct dAoR values: $dAoR_{top}$, $dAoR_{centre}$, and $dAoR_{bottom}$. Note that the GranuDrum frame-by-frame analysis is averaged over 100 frames per measurement.

Cohesive Index

The dynamic angle of repose represents the shape of the slope, but the cohesive index (CI) is a measure of the temporal fluctuations in the flow behaviour [51]. It quantifies flowability – ranging from excellent to very poor – comparable to the flow function constant of the ring shear tests, according to Table 9. The GranuDrum automatically calculates the CI in two steps. First, the standard deviation $\Psi(x)$ to the average interface $\overline{y}(x)$ is calculated using Eq. (4):

$$\Psi(x) = \sqrt{\frac{\sum^{N_y(x)_{k=1}} \left(\overline{y}(x) - y_k(x)\right)^2}{N_y(x)}} \tag{4}$$

where $N_y(x)$ is the number of y-coordinates corresponding to each value of x. If the material is non-cohesive, $N_y(x)$=K=100 is the total number of frames, but for cohesive flow, $N_y(x)$ can be higher ($N_y(x)$>K). Using the standard deviation, the cohesive index is calculated according to Eq. (5):

$$CI = \frac{\sum_x \Psi(x)}{D_{crop}} \tag{5}$$

where D_{crop} is the cropped width of the drum image used for analysis, here set to 79.8 mm (95% of the drum diameter), also shown in Fig. 12.

Flow Regimes

Granular flow in a rotating drum can be described at two distinct scales. At the global scale, we can classify the overall flow state of the

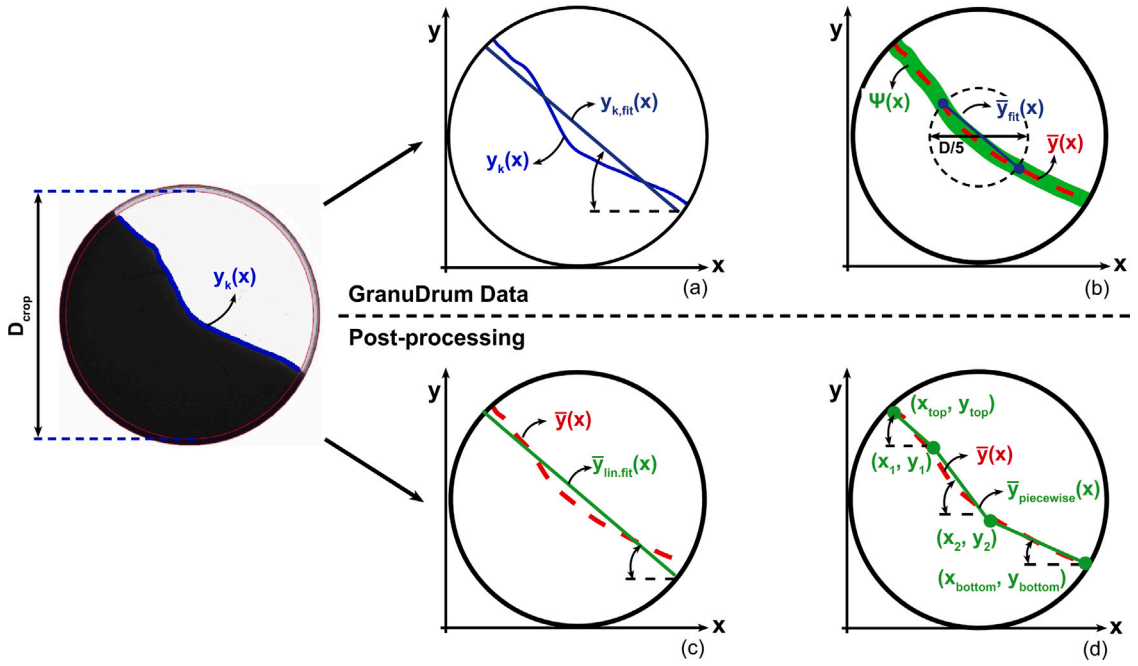

Fig. 12. Rotating drum analysis methods with (a) frame-by-frame analysis, (b) partial fit (both provided by the software of the GranuDrum), (c) linear fit, and (d) piecewise linear fit (proposed in this work).

$$y_{piecewise}(x) = \begin{cases} y_{top} + \dfrac{y_1 - y_{top}}{x_1 - x_{top}}(x - x_{top}) & \text{for } x_{top} \le x < x_1 \rightarrow \mathrm{dAoR}_{top} = \tan^{-1}\left(\dfrac{y_{top} - y_1}{x_1 - x_{top}}\right) \\ y_1 + \dfrac{y_2 - y_1}{x_2 - x_1}(x - x_1) & \text{for } x_1 \le x < x_2 \rightarrow \mathrm{dAoR}_{centre} = \tan^{-1}\left(\dfrac{y_1 - y_2}{x_2 - x_1}\right) \\ y_2 + \dfrac{y_{bottom} - y_2}{x_{bottom} - x_2}(x - x_2) & \text{for } x_2 \le x \le x_{bottom} \rightarrow \mathrm{dAoR}_{bottom} = \tan^{-1}\left(\dfrac{y_2 - y_{bottom}}{x_{bottom} - x_2}\right) \end{cases} \quad (3)$$

Box I.

granular bed using macroscopic flow regimes – such as sliding, rolling, and cascading – which are classified by the Froude number (Fr). At the local scale, we can describe the rheological behaviour at specific regions within the flow using local flow regimes, defined by the inertial number I.

The macroscopic flow regimes in rotating drums include seven distinct states: sliding, surging, slumping, rolling, cascading, cataracting, and centrifuging [52]. The dominant regime can be determined using the Froude number Fr [52,53]:

$$\mathrm{Fr} = \sqrt{\frac{\omega^2 \mathrm{D}}{2g}} \quad (6)$$

where D is the diameter of the drum, ω is the rotational speed, and g is the gravitational acceleration. For the GranuDrum with D = 84 mm, and the rotational speed range of 1–60 rpm, the corresponding Froude number ranges from $6.9 \cdot 10^{-3}$ (1 rpm) to $4.1 \cdot 10^{-1}$ (60 rpm). According to Mellmann [52], this range includes the rolling ($10^{-4} < \mathrm{Fr} < 10^{-2}$) and cascading ($10^{-3} < \mathrm{Fr} < 10^{-1}$), suggesting that only these flow regimes could be observed in our experiments.

While Fr defines the global behaviour, the inertial number provides a more local analysis. For example, in a rotating drum operating in the (globally defined) rolling or cascading regime, the material often exhibits dense flow at the surface, with a quasi-static layer underneath [21]. Thus, multiple inertial-number-defined regimes can coexist within a single Froude-number-defined macroscopic regime.

Design of Experiments

Fig. 13 illustrates how the three setups described above – ring shear tests, ledge tests, and rotating drum tests – and the considered effects of operational conditions characterise the flow behaviour of $NaBH_4$ powder and granules. The outputs (metrics) of the experiments are given, and for each experiment, the considered operational conditions are listed. Furthermore, post-experiment material analyses are shown, which indicate whether particle size, moisture content, or both have changed during the experiment. Additionally, the environmental conditions (ambient or controlled) are noted. To confirm that the selected setups can be used to characterise $NaBH_4$ across multiple flow regimes, an estimate of the inertial number, for each setup, is provided in Appendix A. Summarising, our estimations confirm that the ring shear test operates in the quasi-static regime, the ledge test in the dense flow regime, and the rotating drum in both the dense and the gaseous flow regime, depending on the rotational speed.

3. Results

In this section, the results of the experiments and the effects of the considered operational conditions are discussed.

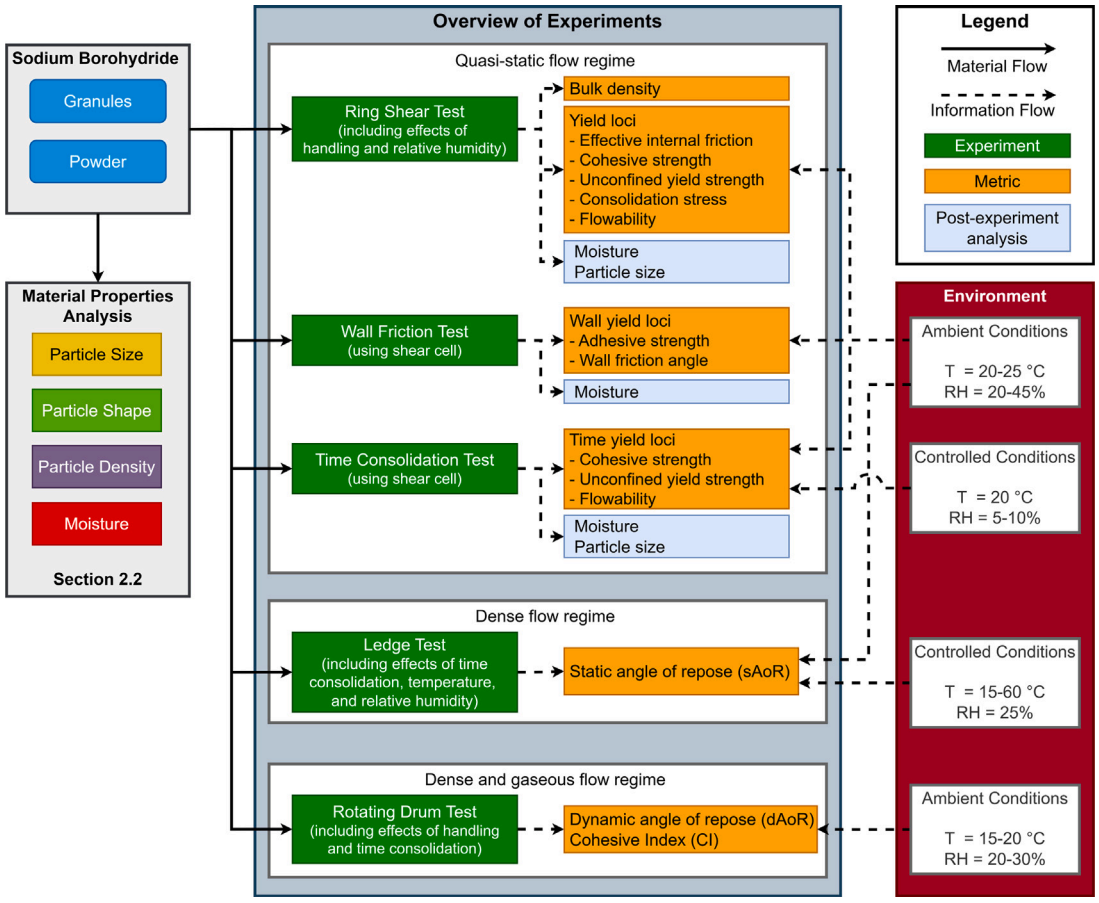

Fig. 13. Overview of experiments to measure the flow behaviour and mechanical characteristics of $NaBH_4$ taking into account operational conditions.

3.1. Ring shear tests

Fig. 14 shows the yield loci of $NaBH_4$ granules and powder, obtained with the Schulze Ring Shear Tester (RST) and the Brooklyn Powder Flow Tester (PFT). Errorbars are used to show the 95% confidence intervals. For both the RST and the PFT results, the yield loci of the powder fall below those of the granules, indicating that a smaller particle size leads to a lower shear stress for the same normal stress ($\tau_{granules}(\sigma) > \tau_{powder}(\sigma)$). Additionally, the slopes of the powder yield loci differ from those of the granules, suggesting that granules experience higher internal friction than powder.

To get more insights, each yield locus is analysed to derive the effective internal friction ϕ_e, cohesion τ_c, bulk density ρ_b, and unconfined yield strength σ_c, and are presented as functions of the consolidation stress σ_1 in Fig. 15. Similar to the yield loci, errorbars represent the 95% confidence interval, also in the x-direction, since σ_1 is derived from the yield loci as well.

First, as indicated by the yield loci, the effective internal friction (Fig. 15(a)) of the granules is consistently higher than that of the powder across the entire stress range ($\phi_{e,granules}(\sigma) > \phi_{e,powder}(\sigma)$). Second, a comparison of the cohesive strength in Fig. 15(b) suggests that the granules are slightly more cohesive than the powder. However, this difference may not be statistically significant when considering the confidence intervals. Third, Fig. 15(c) presents the flow functions of $NaBH_4$, along with reference lines corresponding to flow function constants of 4 and 10. These lines show boundaries for different flow state transitions (Table 4 [45]). When the flow functions of $NaBH_4$ remain below the line with a flow function constant of 10, the material can be classified as free-flowing. Values between 4 and 10 indicate easy-flowing behaviour, while values above 4 suggest cohesive flow. Accordingly, both the granules and the powder exhibit free-flowing behaviour for the entire stress range, except for the granules at the lowest consolidation stress, where they appear easy-flowing. Finally, Fig. 15(d) shows that powder has a higher bulk density than the granules throughout the entire stress range. Additionally, the bulk density of both granules and powder increases with higher consolidation stresses, but powder is more sensitive to this compaction.

Effect of Handling

The effect of handling – breakage and attrition – can be deduced from the particle size distributions measured before and after testing, as shown in Fig. 16. Due to the overlapping confidence intervals, no statistically significant breakage or attrition appears to have occurred. This observation is further supported by Figs. 14 and 15, where both the individual and sequential yield loci and their metrics are shown. The confidence intervals overlap for the yield loci, effective internal friction, cohesion, and flow function, indicating that handling does not significantly alter the mechanical behaviour of the material—i.e., the sample is unaffected by repetitive stress impacts in confined flow.

Only the bulk density (Fig. 15(d)) shows a noticeable difference when comparing individual and sequential ring shear tests. The bulk density of the granules remains approximately constant in the individual tests, while there is a minimal increase during the sequential tests. This could suggest that the repeated loading in sequential tests leads to gradual compaction of the granules, as the samples remain undisturbed in the shear cell between measurements for sequential tests. Consequently, the shear plane may consistently form at the same height within the particle bed, and the combined effects of cell rotation and lid pressure progressively compact the granules above and below this plane. However, the observed change in bulk density is small and, taking into account the confidence intervals, could be regarded as nearly constant. Furthermore, the moisture content of the samples

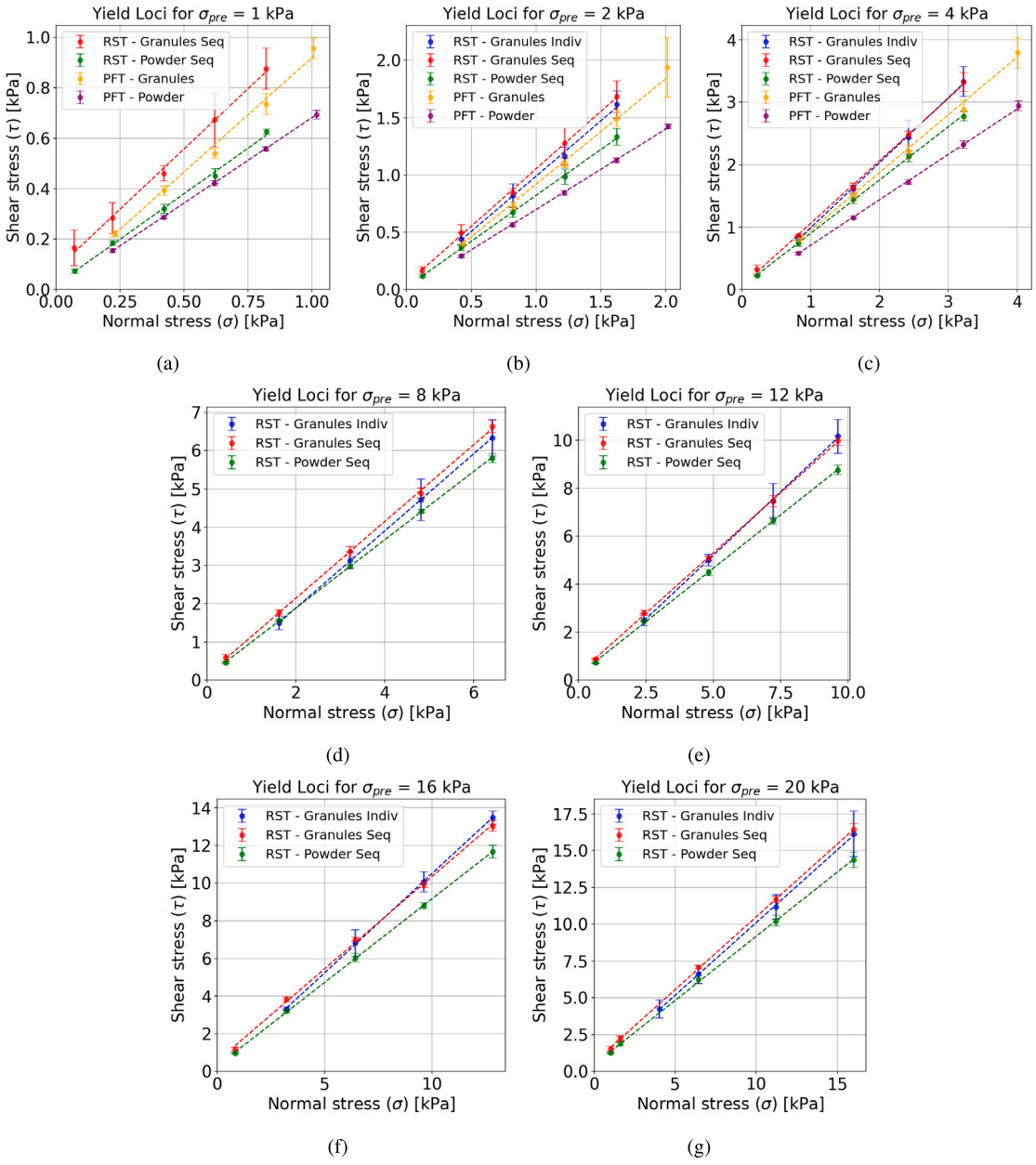

Fig. 14. Yield loci results for $NaBH_4$, errorbars represent the 95% confidence interval.

slightly increases during sequential testing, which could also explain the slight increase in bulk density.

Effect of Relative Humidity

Fig. 17 shows the results of the yield loci for $NaBH_4$ samples with three moisture content levels alongside the yield loci of dry $NaBH_4$. The yield loci for the moisturised samples are measured three times, except for the yield locus with 16 kPa for the samples with 2% moisture, which are only measured twice. Due to the overlapping confidence intervals, no significant effect of moisture can be observed, both for granules and for powder.

Fig. 18 depicts the effective internal friction angle of both powder and granules decreasing with increasing moisture content, except for the granules with 2% moisture, which show no significant effect. Additionally, the cohesive strength increases with increasing moisture content, with powder being more sensitive than granules. The flow functions indicate that, despite these changes, the granules remain free-flowing (except at the lowest consolidation stress for dry granules).

Powder shows higher sensitivity to moisture than granules. While dry powder is free-flowing, all moisture levels result in easy-flowing behaviour at the lowest consolidation stress. At the highest moisture content – 6% – even the second consolidation stress falls within the easy-flowing regime. This trend suggests that above a certain moisture threshold, powder transitions into a cohesive bulk solid.

3.2. *Wall friction tests*

The wall friction tests provide the wall friction angles and adhesion between the $NaBH_4$ samples and the selected wall materials. Adhesion was found to be negligible for all wall materials B, and is therefore not discussed further. Fig. 19 shows the wall friction angles (ϕ_x) for granules and powder, respectively.

For granules, the lowest wall friction angles are observed with stainless steel at low consolidation stresses. However, at stresses exceeding 10 kPa, aluminium yields the lowest wall friction angles. Perspex consistently exhibits the highest wall friction angles for consolidation

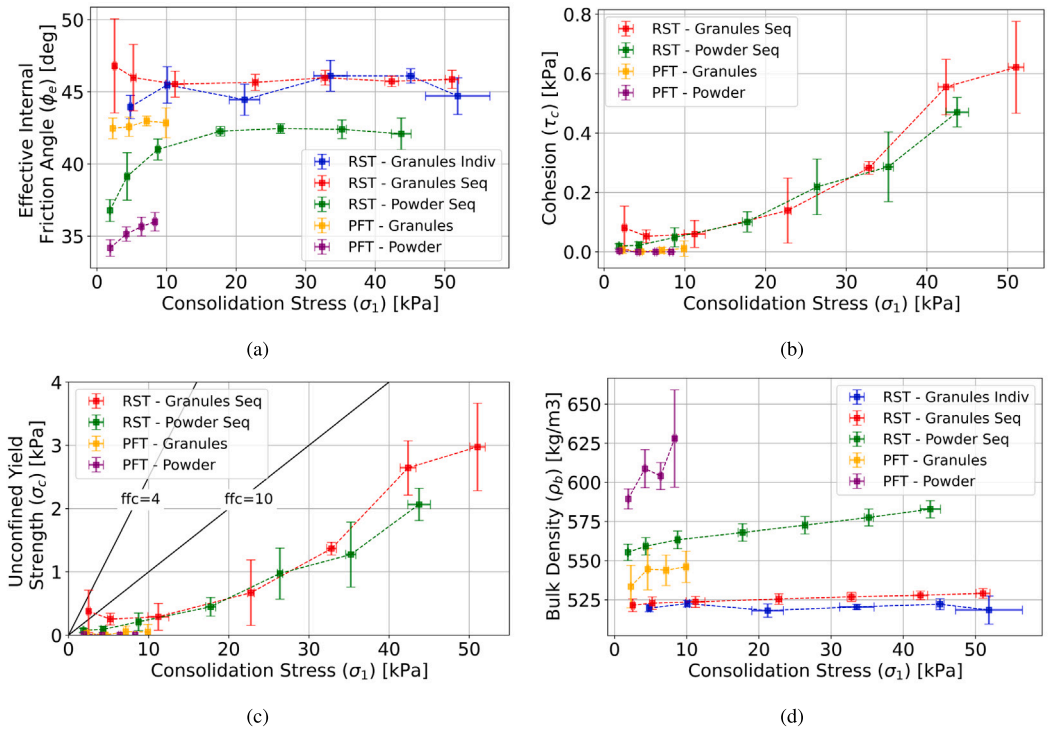

Fig. 15. Effective friction, cohesion, flow functions, and bulk density of $NaBH_4$, errorbars represent the 95% confidence interval.

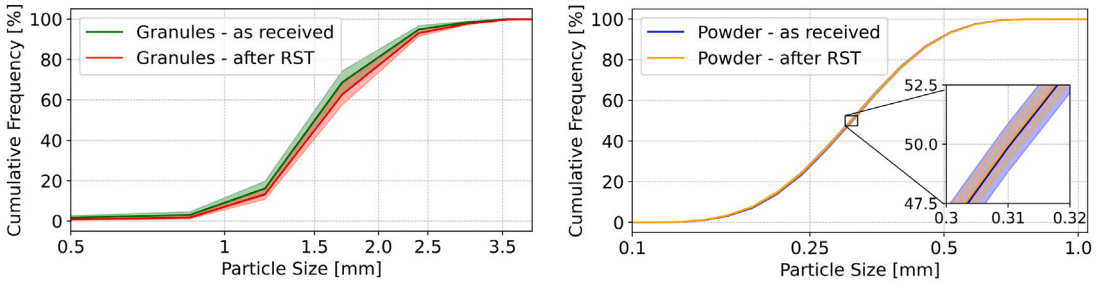

Fig. 16. Effect of handling on the particle size distribution of $NaBH_4$ for (a) granules and (b) powder; coloured bands represent the 95% confidence interval.

stresses up to 30 kPa. At higher stresses the wall friction between stainless steel and granules increases, resulting in no significant difference between stainless steel and perspex.

For powder, the highest wall friction angles are consistently observed with perspex, followed by stainless steel, while the lowest values are recorded for aluminium across all tested consolidation stresses. Furthermore, the wall friction angle asymptotically decreases with consolidation stress. This trend aligns with the observations reported by Larsson [54] for grass powder with a comparable particle size distribution, even for various moisture contents, and by Xanthakis et al. [55] for six metal oxide nanopowders.

Furthermore, the wall friction angle of the powder samples seems negatively correlated to the exerted pressure, approaching an asymptotic value for higher stresses. In contrast, the wall friction angle for the granules seems more or less constant across the entire stress range, except for stainless steel. When comparing the confidence intervals, it is evident that the variability between powder and wall materials is higher than that observed for the granules, and this effect is most pronounced for the stainless steel samples.

Additionally, the surface roughness of the three wall samples was measured, with results presented in Appendix B. Perspex exhibited the smoothest surface, while stainless steel and aluminium showed roughness values approximately six and nine times higher, respectively. Although smoother surfaces typically correspond to lower wall friction, the results in Fig. 19 appear to contradict this trend. Possible explanations include reduced van der Waals forces due to increased surface roughness – effectively increasing the distance between particles and the wall – or the presence of electrostatic forces, particularly relevant for materials like perspex. Particle size also significantly affects these cohesive interactions. However, a comprehensive analysis of the mechanisms underlying the measured wall friction is beyond the scope of this study and will therefore not be further discussed.

3.3. Time consolidation tests

Figs. 20a-d present the results of the time consolidation tests with the Brooklyn PFT for $NaBH_4$ granules. Since a new sample is used for each preshear stress and each consolidation time, the instantaneous yield loci are measured in sixfold. The corresponding uncertainty ranges from 2% to 13% for granules, and 1% to 4% for powder. Therefore, although the time consolidation shear points are only measured once, we are confident that the data can be reliably used for trend analysis.

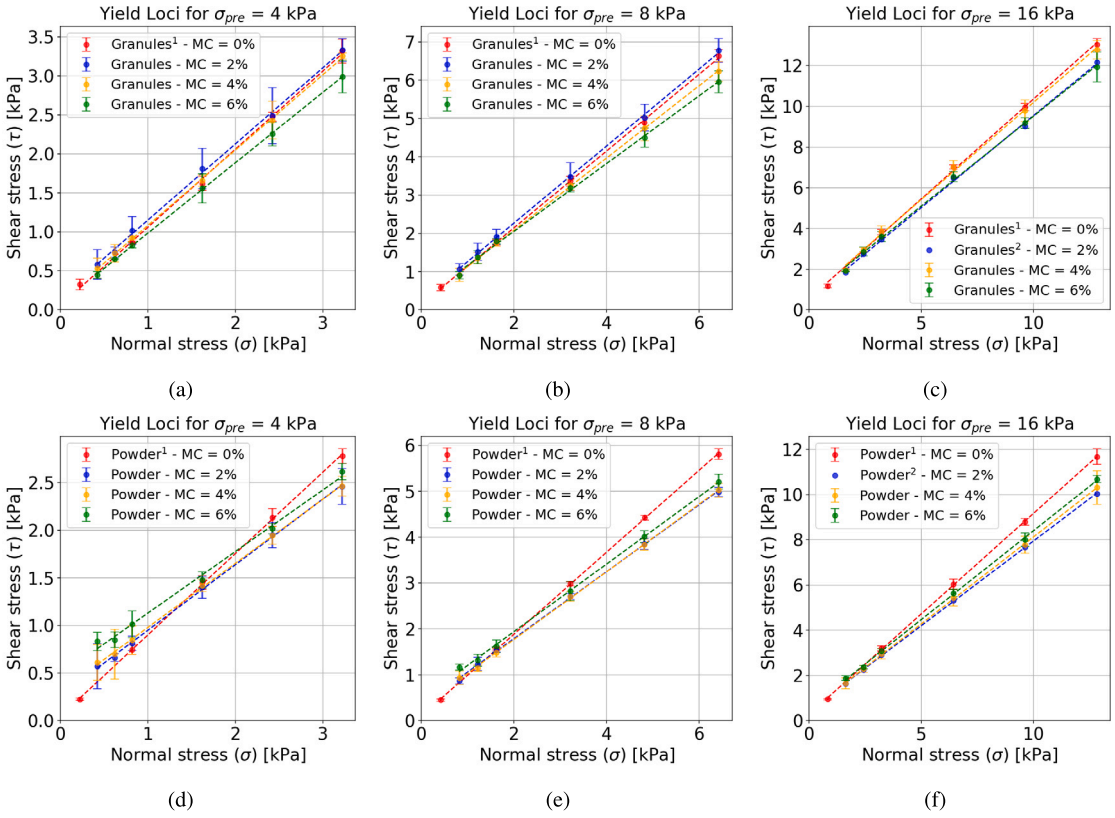

Fig. 17. Yield loci results for $NaBH_4$ with moisture: errorbars represent the 95% confidence interval.
[1]: YL data of sequence tests. Although we denote an assumed moisture content of 0%, this can in practice range between 0.2% to 1% (granules) and 0.2% to 0.6% (powder).
[2]: For the highest preshear stress (16 kPa) for the samples with 2% moisture, only two repetitions are available, and therefore only the mean value is shown.

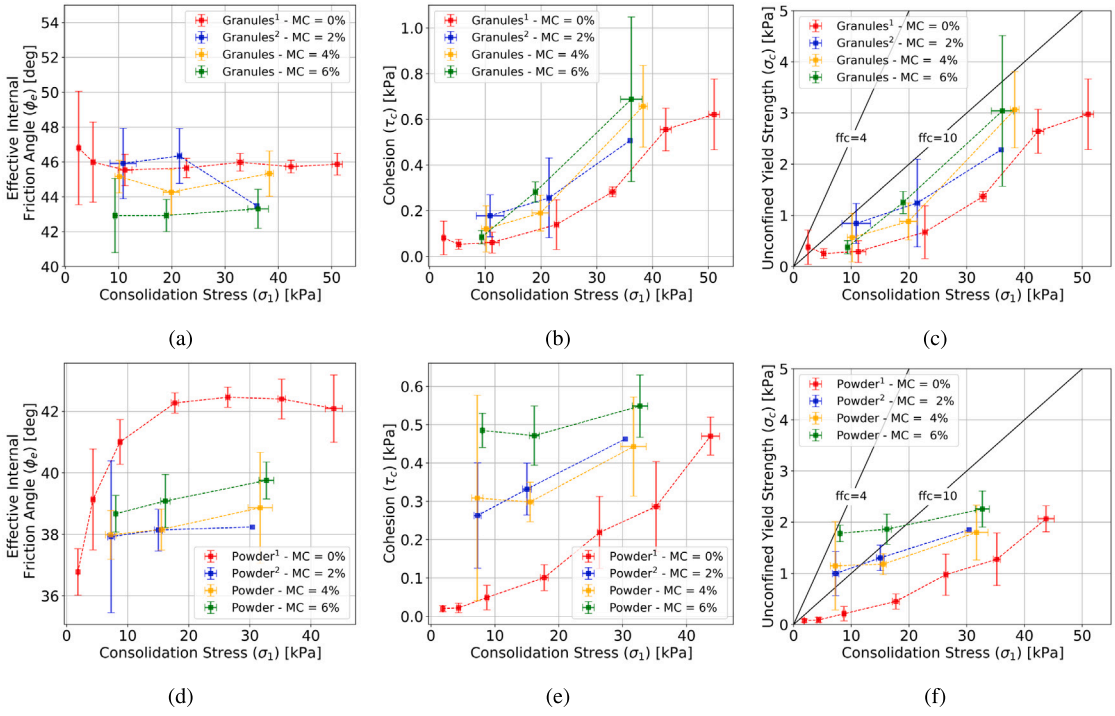

Fig. 18. Effective internal friction, cohesion, and flow functions for $NaBH_4$ with moisture; errorbars represent the 95% confidence interval.
[1]: YL data of sequence tests. Although we denote an assumed moisture content of 0%, this can in practice range between 0.2% to 1% (granules) and 0.2% to 0.6% (powder).
[2]: For the highest consolidation stress for the samples with 2% moisture, only two repetitions are available, and therefore only the mean value is shown.

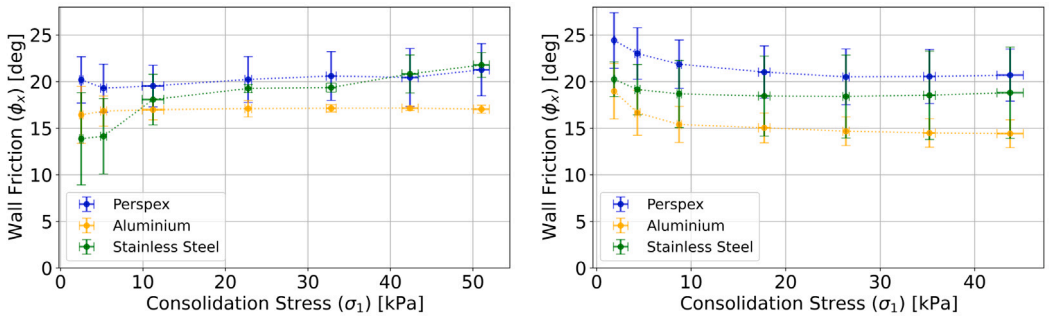

Fig. 19. Wall friction of $NaBH_4$ with perspex, aluminium, and stainless-steel wall samples for (a) granules and (b) powder. Samples slowly absorbed moisture from the ambient air during testing, leading to an increased moisture content from 0.2% (as received) to 0.4% for powder and to 1.3% for granules, on average.

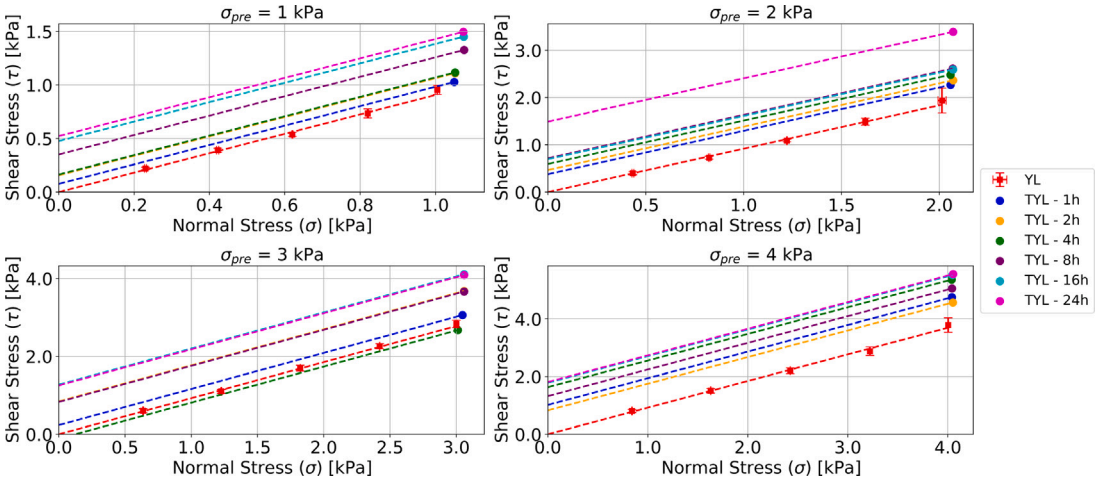

Fig. 20. Time consolidation effects on $NaBH_4$ granules with the Brooklyn Powder Flow Tester.

A clear trend is evident across all preshear stress levels: longer consolidation times generally result in higher shear stress. An exception is observed at the 4-hour consolidation time for the 3 kPa preshear level, where a reduction in shear stress occurs. As this is the sole instance for the granules and no repetitions were performed, this deviation is not considered significant.

Fig. 21 also presents the results of the time consolidation tests for $NaBH_4$ granules, but conducted with the Schulze RST. As with the PFT results, a clear trend is observed: longer consolidation times lead to higher shear stresses. It is worth noting that the standard deviation between the repetitions is relatively large, particularly at longer consolidation times. This is likely due to moisture absorption during the consolidation period.

Since both an elevated moisture content and time consolidation contribute to increased shear strength, it is expected that their combined effect would result in an even greater increase in shear stress. Considering the fluctuating ambient conditions, it is likely that the samples absorbed varying amounts of moisture, which may explain the observed variability in the shear stress response.

Figs. 22a-d present the results of the time consolidation test with the Brooklyn PFT for $NaBH_4$ powder. Whereas the granules showed a clear correlation between consolidation time and shear stress, powder does not consistently follow this trend. In general, longer consolidation times lead to higher shear stresses than non-consolidated powder. However, there are notable exceptions. For instance, a two-hour consolidation period yields higher shear stress than a four-hour period for all preshear levels except 4 kPa. Similarly, the 4-hour and 8-hour consolidation times occasionally result in a greater increase in shear stress than the 24-hour consolidation (see Figs. 22c and 22d).

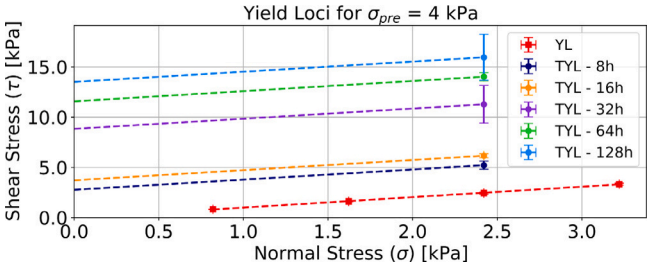

Fig. 21. Time consolidation effects on $NaBH_4$ granules with the Ring Shear Tester. Errobars represent the standard deviation. Post-experiment analysis of the samples showed that moisture absorption for the 128-h consolidated samples was less than 1%, and also no breakage or attrition could be detected.

Fig. 23 presents the flow functions for both granules and powder, obtained by processing the time yield loci, together with the flowability thresholds defined in Table 4. As the time-consolidated granules tested with the Schulze RST were measured only at a single preshear level, flow function constants are shown instead of full flow functions (Fig. 23(a)). Additionally, Fig. 23(b) includes an extra flow function corresponding to a 16-hour consolidation period for a moist powder sample. This sample was taken at a later stage from the same batch of material, during which some caking behaviour was observed. As this was not the case for the previously tested samples, we assume the sample contains a small amount of moisture.

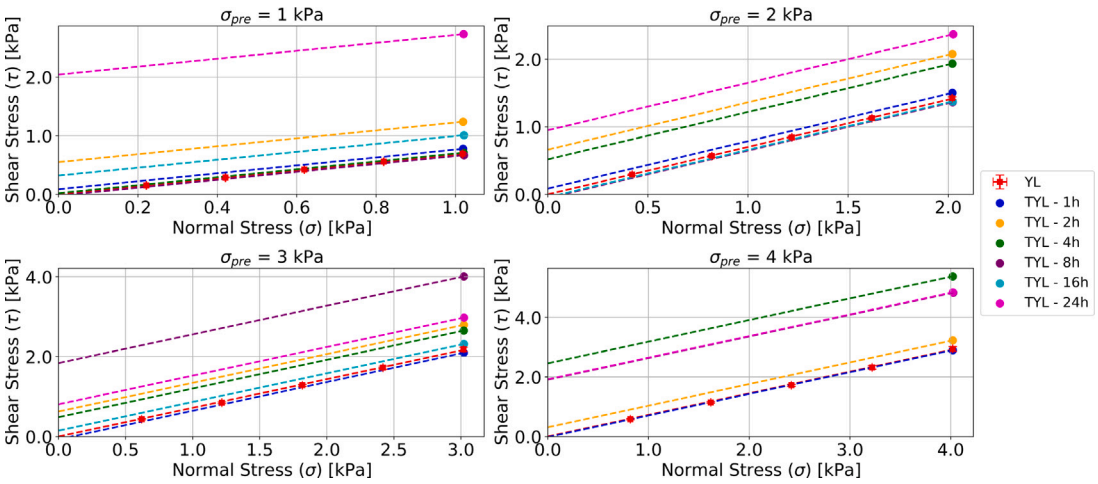

Fig. 22. Time consolidation effects on $NaBH_4$ powder with the Brooklyn Powder Flow Tester. For σ_{pre} - 16 h time consolidation no data is available.

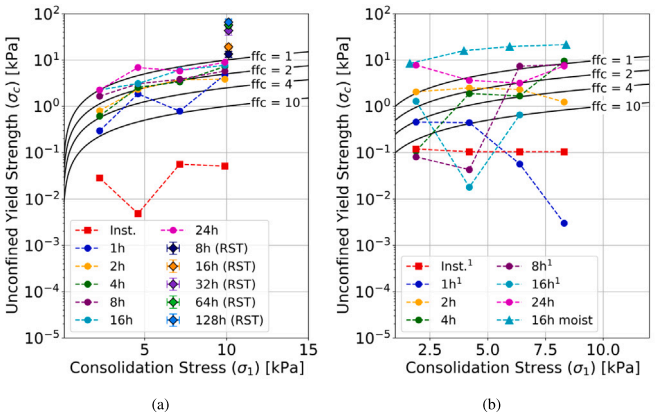

Fig. 23. Time Flow Functions of $NaBH_4$ with the Brooklyn Powder Flow Tester, including Schulze Ring Shear Test (RST) data for (a) granules and (b) powder with moist sample.
[1]: Data has been offset with 0.105 kPa to avoid non-physical negative σ_c values.

Table 10
Angle of repose data of $NaBH_4$ granules and powder.

Measurements	sAoR [deg]	
	Granules	Powder
1	35.46	32.35
2	35.40	32.30
3	34.56	32.15
4	34.59	32.18
5	35.56	32.68
6	34.85	32.31
7	35.02	31.92
8	34.31	32.10
9	34.60	32.35
10	34.93	32.42
Mean	34.93	32.28
Standard Deviation	0.43	0.21
95% Conf. Interval	[34.62 – 35.24]	[32.13 – 32.42]
99.9% Conf. Interval	[34.28 – 35.58]	[31.97 – 32.59]

Similar to the time yield loci results, a clear correlation is observed for the granules – this time between consolidation time, consolidation stress, and unconfined yield strength – where higher stresses or longer consolidation lead to increased unconfined yield strength and thus decreased flowability. This correlation is also evident for the samples tested with the Schulze RST. Additionally, comparing the 8-hour and 16-hour consolidation periods, the compounded effect of moisture and time consolidation appears to be greater than the effect of time consolidation alone. The powder, on the other hand, does not exhibit a clear correlation, and in some cases, a time consolidation period seems to result in improved flowability compared to the non-consolidated samples. However, for the moist sample, a clear increase in unconfined yield strength – thus reduced flowability – is observed, reaching values comparable to those of granules after 16 h of consolidation with the Schulze RST. Fig. 24 illustrates the instantaneous yield loci of the 16-hour consolidated moist powder sample, alongside those of the dry powder samples. The results indicate no significant differences, suggesting that the (limited amount of) absorbed moisture primarily affects the flowability in combination with a period of time consolidation.

Note that the conclusions on time consolidation effects, based on the Brooklyn PFT results, are drawn from a single repetition per condition. While the observed trends are clear, for future research we suggest to include multiple repetitions regarding the time-consolidated shear points.

3.4. Ledge test

The results of the ledge tests are summarised in Table 10. In addition to the static angle of repose for each repetition, the table includes the mean and standard deviation and the 95% and 99.9% confidence intervals. These results indicate that granules exhibit a slightly – but statistically significant – higher sAoR than the powder. During testing, both the granules and the powder showed no cohesive behaviour and formed very linear slopes. To illustrate this, Figs. 25(a) and 25(b) present the mean sAoR and the corresponding confidence intervals for the granules and powder, respectively.

Effect of Time Consolidation

Fig. 26 shows the time consolidation effects on the granules. After 30 min of consolidation under gravity, the material formed a stable column that remained intact even after the partial removal of bottom support (Fig. 26(a)). Collapse occurred only after sufficient material was removed or external energy was applied (e.g., tapping), forming a slope as shown in Fig. 26(b). This behaviour was consistent across consolidation times up to 2 h, indicating the development of weak, reversible cohesion. Once in motion, the material resumed its original free-flowing behaviour, as confirmed by a subsequent standard ledge test.

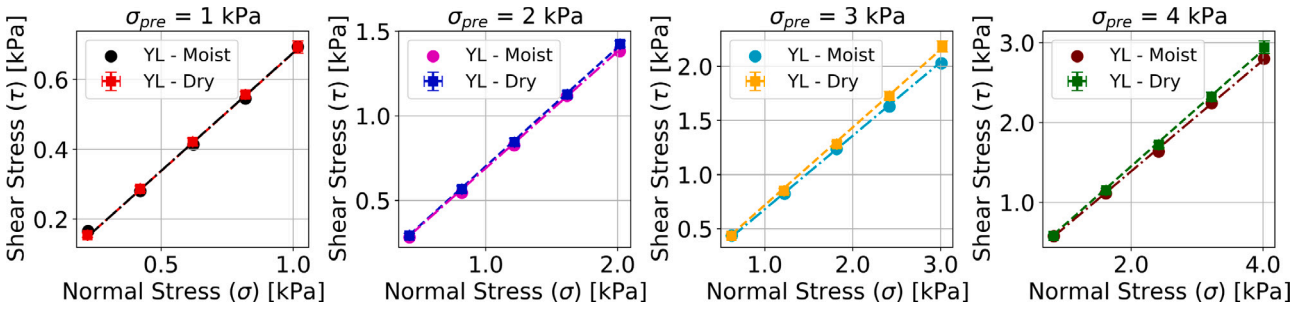

Fig. 24. Instantaneous yield loci of dry and moisturised powder samples.

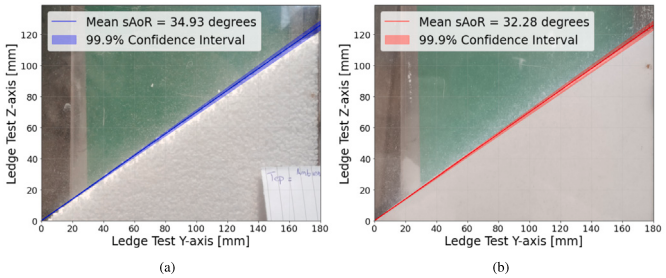

Fig. 25. Projected mean static angle of repose + 99.9% confidence interval on images taken from ledge test experiments with (a) granules and (b) powder.

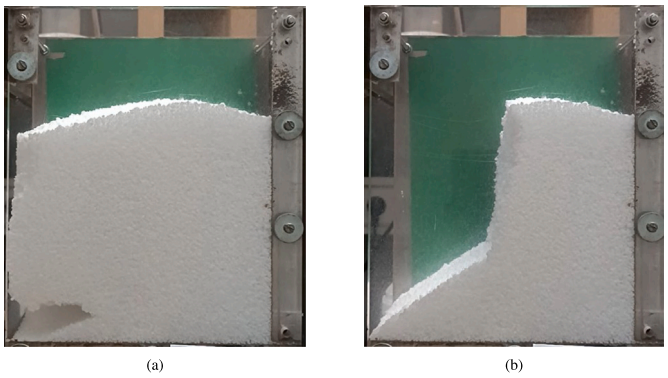

Fig. 26. Time consolidation effect on $NaBH_4$ granules with (a) partial removal of the bottom left particles and (b) collapsed material bed after tapping the ledge box.

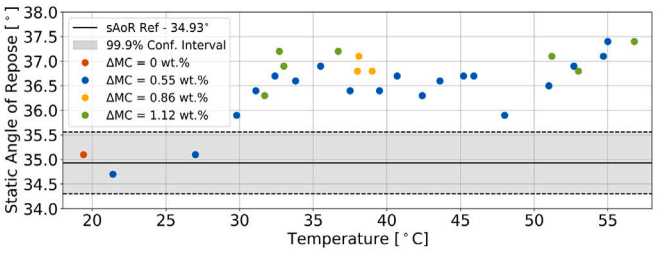

Fig. 27. Effect of temperature and moisture on the static angle of repose of $NaBH_4$ granules. The sAoR reference and corresponding confidence interval illustrate the unconsolidated granules (Table 10).

Effect of Relative Humidity and Temperature

Fig. 27 shows the measured static angle of repose for the different combinations of temperature and moisture, together with the mean sAoR and the 99.9% confidence interval previously obtained, as a reference. For low temperatures (20–27 °C), a slight increase in moisture content has no significant effect on the sAoR, but for higher temperatures, the sAoR increases. However, additional moisture content at these sample temperatures (30–57 °C) does not seem to significantly affect the sAoR. Therefore, we conclude that temperature and moisture affect the angle of repose of $NaBH_4$ granules, but only to a small extent.

3.5. Rotating drum

Fig. 28 shows the average material-air interface $\bar{y}(x)$ and the standard deviation $\Psi(x)$ of both granules (top) and powder (bottom) for the different rotational speeds of the rotating drum. Neither the granules nor the powder shows cohesive behaviour, in line with the ledge test experiments. Also note the transition from a straight slope to an S-shaped slope for the granules as the flow transitions from rolling (low speed) to cascading (high speed). For the powder, such a transition is not clearly visible, but it can be argued that the S-shape is already there for the lowest speed, and the top gets more prominent at increased rotational speeds.

The results of the dynamic angle of repose analysis are presented in Fig. 29a for granules and in Fig. 29b for powder. Each plot shows the mean dAoR across five samples, with errorbars representing the 95% confidence intervals. All approaches consistently show an increasing dAoR with increasing rotational speed, with the exception of the piecewise linear fits. Interestingly, the two inherent GranuDrum methods yield different results: the frame-by-frame analysis closely resembles the linear fit method, while the partial fit analysis results in significantly higher dAoR values—except at 20 rpm, where the dAoRs of both methods converge.

A more detailed representation of the behaviour of $NaBH_4$ in the rotating drum is given by the piecewise linear fits. For the granules, a clear transition is observed at 10 rpm: the top angle sharply drops, the centre angle increases in line with the partial fit, and the bottom angle remains relatively constant. A different pattern is observed for powder. From 1 to 40 rpm, the bottom angle remains consistently lower than the centre angle, which is in turn lower than the top angle. A notable shift occurs at 40 rpm, where the centre angle increases sharply and the top angle decreases. However, when comparing these results to the average interface profiles of Figs. 28g-l, it can be argued that this transition starts already at 20 rpm. This difference may be caused by the sensitivity of the piecewise analysis to the determination of the breakpoints, which are shown in Fig. C.2. Nevertheless, the piecewise method offers a more nuanced view of the surface dynamics than the other approaches, but further research is required to assess its added value and robustness.

The cohesive indices of granules and powder samples are presented in Fig. 30, alongside the applicable flow thresholds defined in Table 9. The granules exhibit good flowability across all rotational speeds,

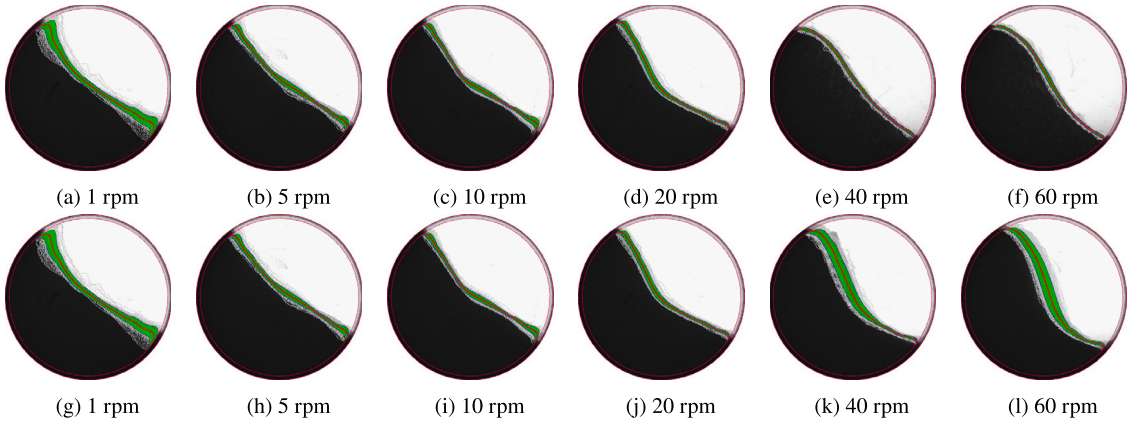

Fig. 28. Average material-air interfaces with standard deviation of $NaBH_4$ samples for varying rotational speeds with (a–f) granules and (g–l) powder. Images are provided by the GranuDrum.

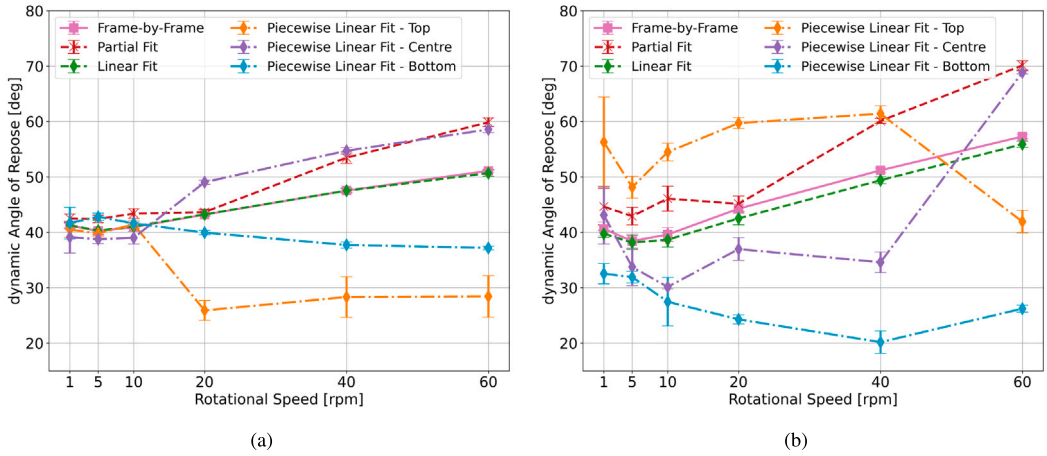

Fig. 29. Dynamic Angle of Repose of $NaBH_4$ as a function of increasing rotational speed for (a) granules and (b) powder. Both figures show mean values over the samples with errorbars representing the 95% confidence interval.

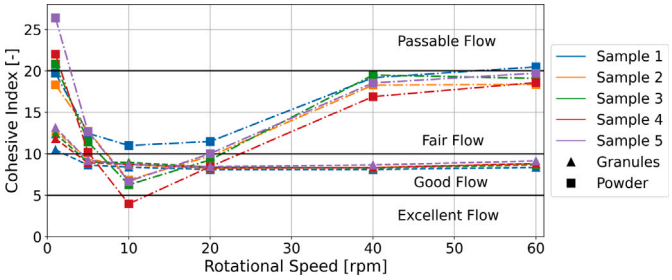

Fig. 30. Cohesive indices of $NaBH_4$ samples as a function of increasing rotational speed.

except at 1 rpm, where the flow is classified as fair. In contrast, powder behaves significantly differently. The flow is fair-passable for the lowest speed, improves to fair-good, and some samples even reach excellent flow at 10 rpm. However, at higher rotational speeds, all powder samples show a decline in flowability, returning to fair flow.

Effect of Handling

The effect of handling – hysteresis – on the dynamic angle of repose can be seen in Fig. 31. Positive hysteresis indicates the angle of repose increases with repeated rotation and vice versa. The exact hysteresis effects depend on the type of analysis; neither shows significant hysteresis effects, and therefore, the effect of handling on the dynamic angle of repose is not investigated further.

The cohesive indices (Fig. 32) show no hysteresis effect for granules and show a slight effect for powder, with a lower cohesive index across the entire speed range. Still, this effect is very small, and except for 20 rpm, the flow does not classify differently.

Effect of Time Consolidation

The effects of 10 min of consolidation on the flow of $NaBH_4$ in the rotating drum are shown in Fig. 33 for granules and Fig. 34 for powder. For the granules, the evolution of the flow from 0.2 to 20 s, along with the average flow over this time range, indicates no significant effect of time consolidation. In contrast, the powder is strongly affected: during the first 20 s of rotation, the flow appears highly cohesive and agglomerated. However, from 21 to 40 s, the flow transitions, effectively losing the cohesiveness and agglomerates gained by the time consolidation period. This trend is further supported by the average flow profiles shown in Figs. 34(f) and 34(l), which confirm that the cohesive strength gained by the time consolidation diminishes once flow is initiated.

Figs. 35a and 35b present the dAoR as a function of rotation time for granules and powder, respectively, based on the GranuDrum's frame-by-frame analysis. The plots show the mean and confidence interval

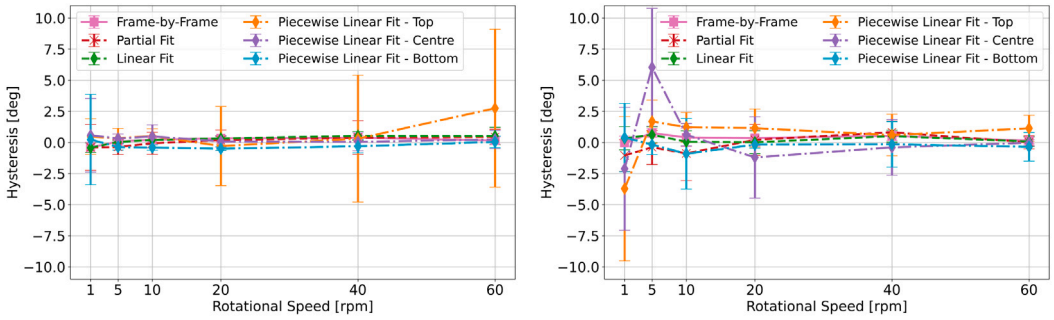

Fig. 31. Hysteresis of the dAoR of $NaBH_4$ as a function of increasing rotational speed for (a) granules and (b) powder. Both figures show mean values over the samples with errorbars representing the 95% confidence interval.

Table 11
Effect of drum rotation on the cohesive indices of time-consolidated $NaBH_4$ samples.

Material	Consolidation time [min]	Rotation time [s]	Cohesive index [-]	
			Mean	95% Confidence interval
Granules	0	20	12.13	1.29
	5	20	12.31	1.25
	5	40	12.09	1.70
	10	20	12.39	0.749
	10	40	12.97	0.913
Powder	0	20	21.46	3.83
	5	20	37.06	10.2
	5	40	24.81	5.17
	10	20	50.18	16.7
	10	40	25.86	5.13

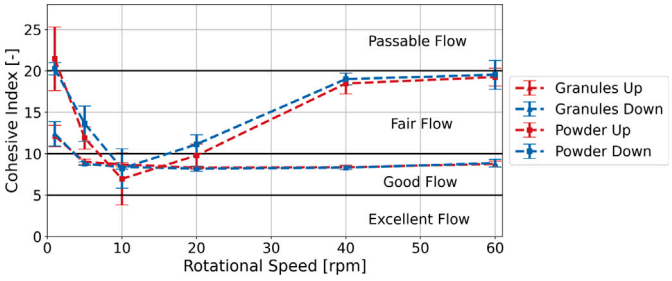

Fig. 32. Hysteresis of the cohesive index of $NaBH_4$ for granules and powder as a function of rotational speed. Sample means are plotted with dashed lines, and errorbars represent the 95% confidence interval.

over the 5 samples for the two time consolidation periods alongside the reference without consolidation.

Additionally, Table 11 summarises the cohesive indices for both materials over the 0–20 s and 20–40 s intervals, following 5 and 10 min of consolidation. The results confirm the visual observations: time consolidation has a negligible effect on the granules, while powder initially exhibits increased cohesion that rapidly dissipates during rotation. Notably, although the powder appears to regain its original behaviour after 40 s, the cohesive index suggests some residual cohesion may persist.

3.6. Moisture analysis

For none of the shear tests conducted with the Schulze Ring Shear Tester was a climate chamber available, and ambient conditions varied considerably—ranging from 20–25 °C and 20%–45% RH—during testing, exceeding the moisture absorption limits of $NaBH_4$. To quantify moisture uptake during testing, samples were analysed post-experiment following the ASTM *Standard Test Method for Total Evaporable Moisture Content of Aggregate by Drying*. According to the supplier (CPH Chemicals), the maximum moisture content of the samples was 0.3%, which was confirmed by measurements of 0.22% for the granules and 0.19% for the powder before testing.

For the sequential and individual ring shear tests, the moisture content ranged from 0.51 to 1.03% for the granules and 0.26% to 0.58% for the powder. For the wall friction test, the moisture content ranged from 0.42% to 1.31% for the granules and was 0.18% for the powder. Finally, the moisture contents measured after the time consolidation tests for granules ranged from 0.65% to 0.77%.

To validate that the added moisture due to absorption from ambient air did not chemically affect the samples, XRD measurements were performed on $NaBH_4$ powder in two conditions: as received and after undergoing deliquescence due to moisture absorption followed by drying at 50 °C. The results, presented in Appendix D, show no detectable presence of $NaBO_2$, confirming that the material remained chemically unchanged after moisture absorption and subsequent drying.

4. Implications for bunkering equipment

Three flow regimes have been examined, along with the effect of operational conditions including handling-induced stresses, extended storage periods, and variations in ambient temperature and humidity. Consequently, this section discusses the results of the experiments in terms of their implications for the bunkering of $NaBH_4$, with a particular focus on the design of typical storage and handling equipment.

4.1. Storage equipment: Silos and hoppers

Storage equipment for bulk solids such as $NaBH_4$ includes hopper silos, where all three flow regimes – gaseous, dense, and quasi-static –

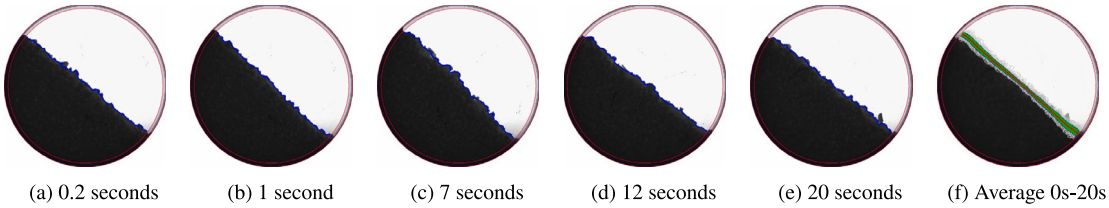

Fig. 33. Material–air interfaces for a 10 min consolidated $NaBH_4$ granules sample with (a–e) the first 20 s of flow and (f) the average interface with standard deviation. Images are provided by the GranuDrum.

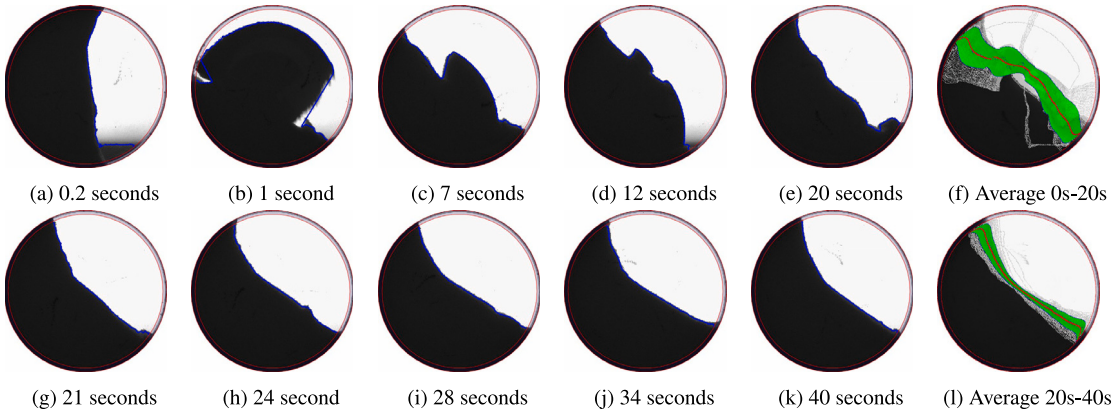

Fig. 34. Material–air interfaces for a 10 min consolidated $NaBH_4$ powder sample with (a–e) the first 20 s of flow, (f) average interface with standard deviation of the first 20 s, (g–k) the last 20 s of flow, and (l) average interface with standard deviation of the last 20 s. Images are provided by the GranuDrum.

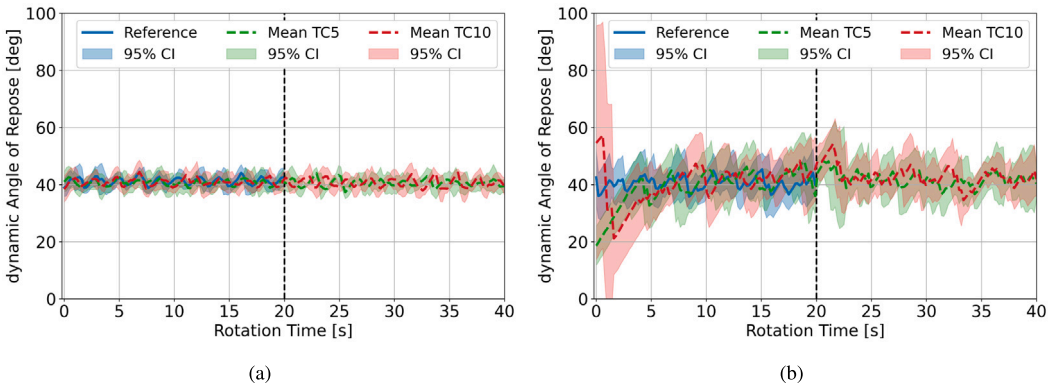

Fig. 35. Effect of drum rotation (1 rpm) on the dynamic angle of repose of time consolidation $NaBH_4$ for (a) granules and (b) powder.

can be encountered. Gaseous flow typically occurs at the inlet, while dense or quasi-static flow is more pronounced within the silo and at the outlet, depending on, e.g., the geometry of the hopper silo. The experimental results of the rotating drum (gaseous and dense flow), ledge test (dense flow) and ring shear tests (quasi-static flow) indicate that dry, unconsolidated $NaBH_4$ exhibits consistent and favourable flowability across all regimes.

The quasi-static flow behaviour, characterised with ring shear tests, showed minimal cohesion for both granules and powder. Granules presented a stress-independent effective angle of internal friction, while the powder showed a nonlinear increase with consolidation stress. This trend might be attributed to the increasing bulk density of the powder under load, potentially leading to enhanced interparticle friction. Interestingly, granules exhibited a higher effective angle of internal friction than powder, while their bulk density was lower. This could be explained by differences in particle shape: the powder was found to be slightly more convex and circular, which has been correlated with a reduction in friction by Yu et al. [56] and Nie et al. [57].

Time consolidation proved a critical factor in storage design, particularly for granules, which showed a clear increase in unconfined yield strength—and thus reduced flowability—with increased consolidation stress and time, causing the material to transition from free-flowing to cohesive behaviour. However, the rotating drum experiments showed that the added cohesion due to time consolidation was dissipated by simply rotating the drum at low speeds. This indicates that shore-based and onboard storage equipment may require external means of agitation to break the cohesive bonds gained during longer storage periods. However, further research is needed to confirm this hypothesis. Additionally, based on the measured characteristics with the ring shear tests, e.g., unconfined yield strength, wall friction, and effective

internal friction, initial silo and hopper dimensions can be estimated using guidelines outlined in [45].

Relative humidity is another key operational parameter. $NaBH_4$ is known to be hygroscopic, and experiments showed that both powder and granules absorbed moisture at relative humidities above 25% at room temperature, and as low as 10% for elevated temperatures (55 and 85 °C). While absorbed moisture was shown to have no significant effect on the instantaneous flowability and corresponding characteristics, it significantly accelerated the consolidation effects measured with both the Schulze RST and the Brooklyn PFT. This suggests that humidity control measures should be incorporated in storage equipment design to avoid compromised flowability for long-term storage periods. Additionally, silo condensation, a problem in environments with large temperature fluctuations [58], can accelerate moisture uptake and should be mitigated through e.g., insulation, ventilation, or dehumidification systems.

In summary, while dry, unconsolidated $NaBH_4$ demonstrates favourable flow characteristics, the design of storage equipment must account for time consolidation effects and the material's inherent hygroscopicity. Silo geometry, environmental control, and agitation mechanisms are essential to ensure reliable discharge and prevent flow obstructions over time.

4.2. Handling equipment: Conveyors

Handling equipment can be broadly categorised into mechanical and pneumatic conveying systems, each associated with different flow regimes and operational conditions.

In mechanical systems, such as a belt or chain conveyor, the quasi-static flow regime dominates at low speeds, transitioning to dense flow for higher throughput. Granules and powder showed similar behaviour in both regimes, with minimal cohesion and consistent flowability. Furthermore, no significant attrition or breakage was measured in the experiments, indicating that both powder and granules can withstand the simulated handling stresses. The rotating drum experiments showed that granules exhibit less temporal fluctuations compared to powder, which could be advantageous for maintaining steady transport in mechanical conveyor systems. Additionally, the dynamic angle of repose of granules was consistently lower than that of powder across all tested rotational speeds, while the granules had a higher static angle of repose with the ledge test. This highlights the importance of distinguishing between static and dynamic flow behaviour when designing handling equipment.

Time consolidation effects are, by definition, not applicable while material is in motion. However, after idle periods – particularly those in the range of hours – consolidation effects may become significant, particularly for powder, as shown with the rotating drum experiments. Increased cohesion during these periods could lead to elevated torque requirements or even blockages upon restart. Therefore, it is recommended that mechanical conveyors be emptied after use or designed to minimise material residence time during downtime.

Pneumatic conveying systems, which rely on over- or under-pressure to transport materials, can operate in either dense or gaseous regimes, depending on the system configuration. However, the presence of moisture in the transport medium (air or gas) can result in moisture uptake by $NaBH_4$ if temperature and relative humidity conditions are not sufficiently low. While $NaBH_4$ demonstrated mostly good to fair flowability in the rotating drum – operating primarily in the dense flow regime and approaching gaseous flow for higher speeds – these conditions do not fully replicate the high-velocity, turbulent flow typical for pneumatic systems. Therefore, more research is required for the flow of $NaBH_4$ under realistic pneumatic conveying conditions.

Similar to storage systems, humidity control is also essential in handling equipment. $NaBH_4$'s hygroscopic nature means that even short-term exposure to elevated moisture content can accelerate time consolidation effects, potentially leading to reduced flowability. To mitigate these risks, all conveying solutions should be equipped with air-drying systems to maintain low humidity levels.

5. Conclusion

This study experimentally determined and discussed the relevant mechanical characteristics and flow behaviour of sodium borohydride to enable its use as a granular fuel for maritime vessels. Both granules and powder demonstrated favourable flowability across quasi-static, dense, and gaseous regimes under dry (RH < 25% at 20 °C), unconsolidated conditions. However, flowability and mechanical characteristics are significantly affected by operational conditions, which must be carefully considered in the design of storage and handling systems.

Time consolidation emerged as a critical factor based on the experiments, particularly for granules, which transitioned from free-flowing to cohesive and eventually to non-flowing behaviour under prolonged consolidation periods, with a strong relationship between flowability, storage time, and stress. Powder showed a similar trend, albeit less pronounced. The presence of even small amounts of absorbed moisture increased these effects, with both powder and granules becoming non-flowing after 16 h of consolidation. However, these effects can be reversed through agitation, suggesting that storage systems should incorporate agitation mechanisms. Consequently, the design of such systems should be informed by time consolidation data to ensure reliable discharge.

Relative humidity and temperature are also key parameters. $NaBH_4$ is hygroscopic, absorbing moisture at humidity levels exceeding 25% RH at room temperature or as low as 10%–15% RH at elevated temperatures (55–85 °C). Based on the conducted experiments, low moisture contents do not significantly affect flowability and mechanical characteristics during handling. However, even small amounts of absorbed moisture were found to accelerate time consolidation effects, resulting in a more rapid decline in flowability over time. Additionally, temperature fluctuations can lead to condensation on equipment walls, effectively increasing the relative humidity within the equipment. These findings highlight the importance of humidity control in both storage and handling systems for $NaBH_4$.

Handling, including repetitive loading, affects the flowability and characteristics of $NaBH_4$ only slightly. Granules were virtually unaffected, while powder exhibited an increase in effective internal friction and bulk density with increasing consolidation stress. Although material in handling systems is typically in motion – mitigating the risk of time consolidation – idle periods may cause time consolidation effects to develop, potentially increasing cohesion and reducing flowability. As a precaution, handling equipment should be emptied during downtime to prevent startup issues. Furthermore, the experiments used in this study are not sufficiently representative for pneumatic conveying due to the absence of high-speed experiments. Therefore, additional research is required to assess the behaviour of $NaBH_4$ for pneumatic conveying systems.

In summary, while $NaBH_4$ shows excellent flow characteristics for dry and unconsolidated conditions, its sensitivity to time consolidation and moisture necessitates a design approach that integrates environmental control and agitation mechanisms to ensure consistent and reliable flow across all operational scenarios.

CRediT authorship contribution statement

M.C. van Benten: Writing – original draft, Visualization, Methodology, Formal analysis, Data curation, Conceptualization. **J.T. Padding:** Writing – review & editing, Supervision, Funding acquisition. **D.L. Schott:** Writing – review & editing, Supervision, Funding acquisition.

Declaration of competing interest

The authors declare that they have no known competing financial interests or personal relationships that could have appeared to influence the work reported in this paper.

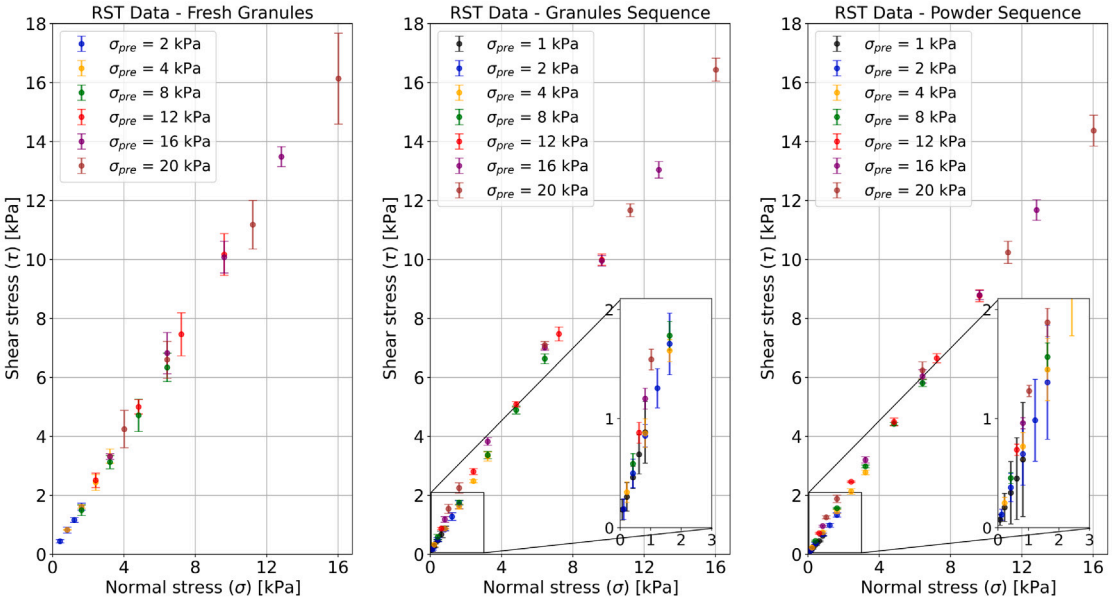

Fig. B.1. Yield loci data of $NaBH_4$ using the Schulze Ring Shear Tester for (a) granules individual yield loci, (b) granules sequential yield loci, and (c) powder sequential yield loci.

Acknowledgements

This work is part of the project SH2IPDRIVE with project number MOB21013, funded by the Ministry of Economic Affairs and Climate Policy, RDM regulation, carried out by the Netherlands Enterprise Agency. Part of the experiments presented in this work were carried out by Delft Solids Solutions, and for part of the experiments, a climate chamber at TNO was used. The $NaBH_4$ samples with elevated moisture content and the corresponding ring shear tests were prepared and conducted by Bjørn Romijn as part of his MSc program in Mechanical Engineering. We would like to thank Gabrie Meesters for enabling the rotating drum experiments, for the insightful discussions on the behaviour of $NaBH_4$, and for assisting with the XRD measurements carried out by Jurre Maaskant as part of his BSc program in Chemical Engineering.

Appendix A. Estimation of inertial number

A.1. Ring shear tests

For the ring shear tests, the inertial number has to be calculated using the formulation for confined flows. We use the lowest normal pressure and the particle size d equal to the mean size of the $NaBH_4$ granules to ensure an upper bound for I is provided. The shear rate $\dot{\gamma}$ is equal to the ratio of the shear velocity (1.5 mm/min) to the height h of the shear zone. Assuming a shear zone of 2–3 particles, $h \approx 5$ mm. This results in the following estimation of the inertial number:

$$I = \frac{\dot{\gamma} d}{\sqrt{\sigma/\rho}} = \frac{\frac{v}{h} d}{\sqrt{\sigma/\rho}} = \frac{\frac{1.5 \cdot 10^{-3}}{60 \cdot 5 \cdot 10^{-3}} \cdot 1.8 \cdot 10^{-3}}{\sqrt{200/1047}} = 2.06 \cdot 10^{-5} \quad (7)$$

As the upper estimate of I is in the order of 10^{-5}, we can safely assume that all ring shear tests operate in the quasi-static regime.

A.2. Ledge test

For the ledge tests, the inertial number has to be calculated using the formulation for free-surface flow, and as such, we need to estimate the flowing layer thickness h and the average velocity of this layer $\bar{V}$.

Visual observation during the experiments with the granules showed that after opening the hatch, a flowing layer of 5–10 particles, which gradually thinned to 3–5 particles towards the end of the discharge period, can be identified. The average flow velocity on the other hand requires more steps to estimate. For most repetitions, approximately 60% of the total 1.9 kg was discharged in 6.5 s, yielding a mass flow rate of $\dot{m} = 0.6 \cdot 1.9/6.5 = 0.18$ kg/s on average. The shear surface S can be averaged at $S = \text{length} \cdot \text{width}/\cos(\text{sAoR}) \approx 0.183 \cdot 0.1/\cos(33.5°) = 0.022$ m^2. Finally, assuming an average bulk density ρ_b of 500 kg/m^3, this gives an approximate average velocity $\bar{V} = \dot{m}/(\rho_b \cdot S) = 0.18/(500 \cdot 0.022) = 0.0164$ m/s. Substituting the average sAoR of granules and powder for θ, we find that the inertial number can be estimated as:

$$I = \frac{5}{2} \frac{\bar{V} d}{h\sqrt{ghcos(\theta)}} = \frac{5}{2} \frac{0.0164 \cdot 1.8 \cdot 10^{-3}}{5 \cdot 1.8 \cdot 10^{-3}\sqrt{9.81 \cdot 5 \cdot 1.8 \cdot 10^{-3} \cdot \cos(33.5°)}} \approx 3 \cdot 10^{-2} \quad (8)$$

for the granules. For the powder it is unclear from what the flowing layer thickness will be. The powder particles will likely move in clumps, but this is not clearly visible from the experiments. If we assume that both d and h scale with the ratio of $d_{powder}/d_{granules} \approx 0.33/1.8 = 0.183$, then I_{powder} can be estimated as $I_{granules} \cdot 0.183/0.183^{1.5} \approx 0.07$, which is also the dense flow regime. Thus, we can assume the ledge test operates in the dense flow regime – as expected – for both the granules and the powder.

A.3. Rotating drum

Two estimates of the inertial number can be determined for the rotating drum simulations: a lower estimate for 1 rpm and a higher estimate for 60 rpm. Similar to the ledge tests, the inertial number has to be calculated for free-surface flows, and hence the flowing layer thickness h and average velocity $\bar{V}$ have to be estimated.

The flowing layer thickness is estimated using the work of Félix et al. [59], who identified the h/d ratio for various drum to particle ratios (D/d and W/d, where D is the drum diameter and W the drum width) and rotational speeds. For granules with an average size of 1.8 mm, D/d = 46.6 and W/d = 11.11, yielding a corresponding h/d of approximately 5 for 1 rpm. . For powder with an average size of

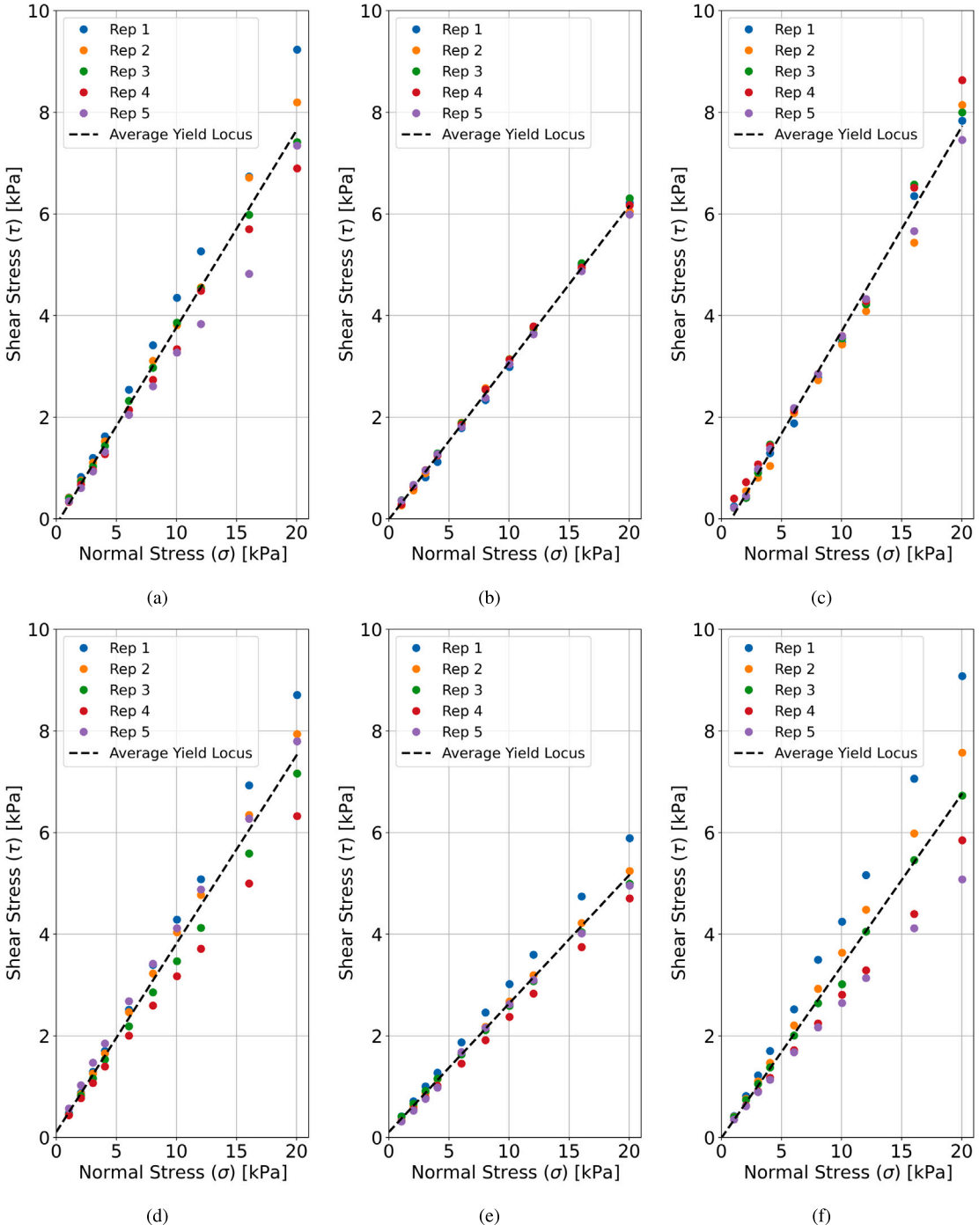

Fig. B.2. Wall yield loci data of $NaBH_4$ using the Schulze Ring Shear Tester for (a) granules-perspex, (b) granules-aluminium, (c) granules-stainless steel, (d) powder-perspex, (e) powder-aluminium, and (f) powder-stainless steel.

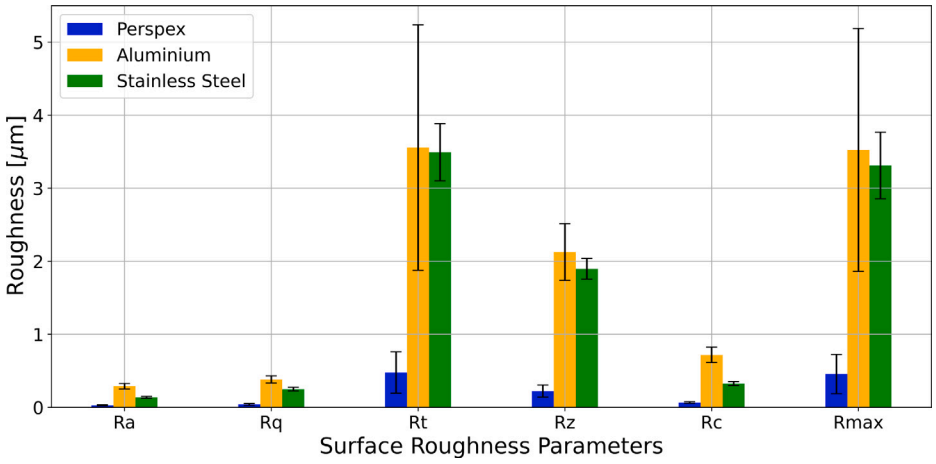

Fig. B.3. Measured wall surface roughness parameters of perspex, aluminium, and stainless steel wall samples, n = 16, errorbars represent 95% confidence intervals.

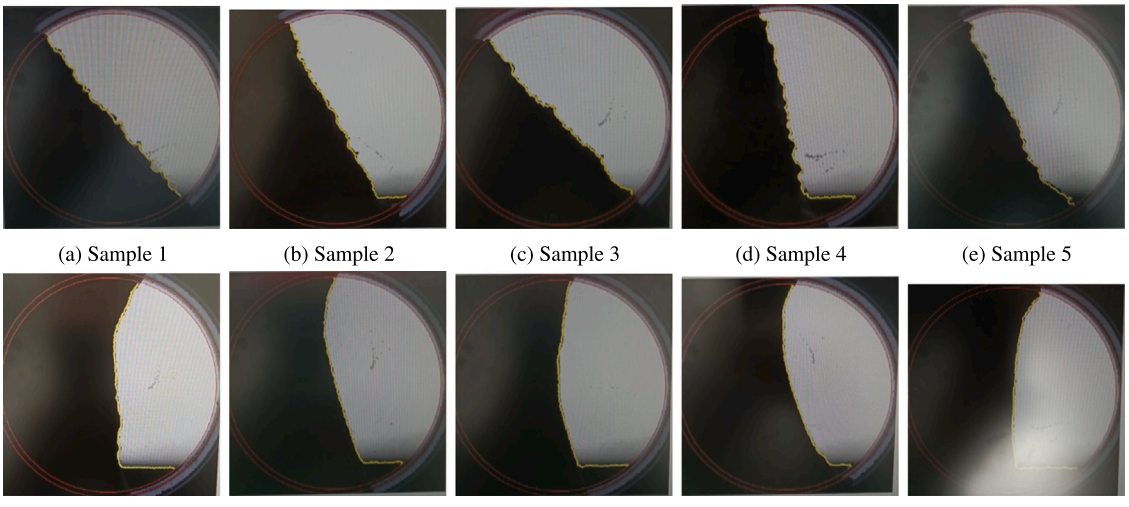

(a) Sample 1 (b) Sample 2 (c) Sample 3 (d) Sample 4 (e) Sample 5

(f) Sample 1 (g) Sample 2 (h) Sample 3 (i) Sample 4 (j) Sample 5

Fig. C.1. Snapshots of rotating drum with $NaBH_4$ samples after 10 min of consolidation, right before material collapses and measurement of the slope starts for (a–e) granules and (f–j) powder.

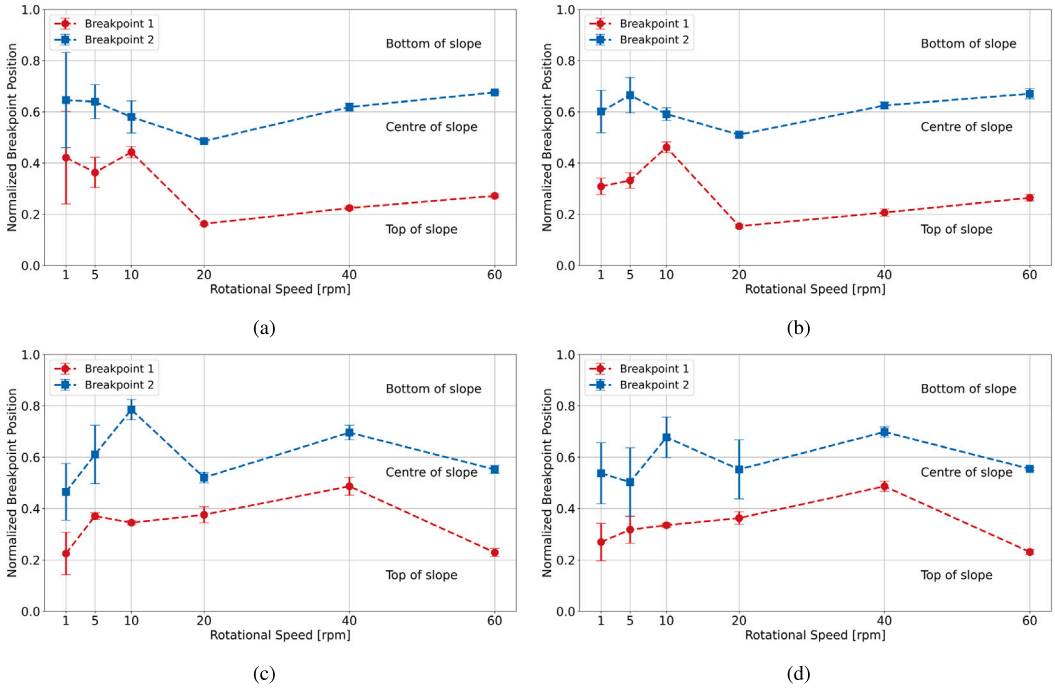

Fig. C.2. Breakpoints for piecewise linear polynomial analysis for the dynamic angle of repose of $NaBH_4$ for (a) granules increasing speed, (b) powder increasing speed, (c) granules decreasing speed, (d) powder decreasing speed.

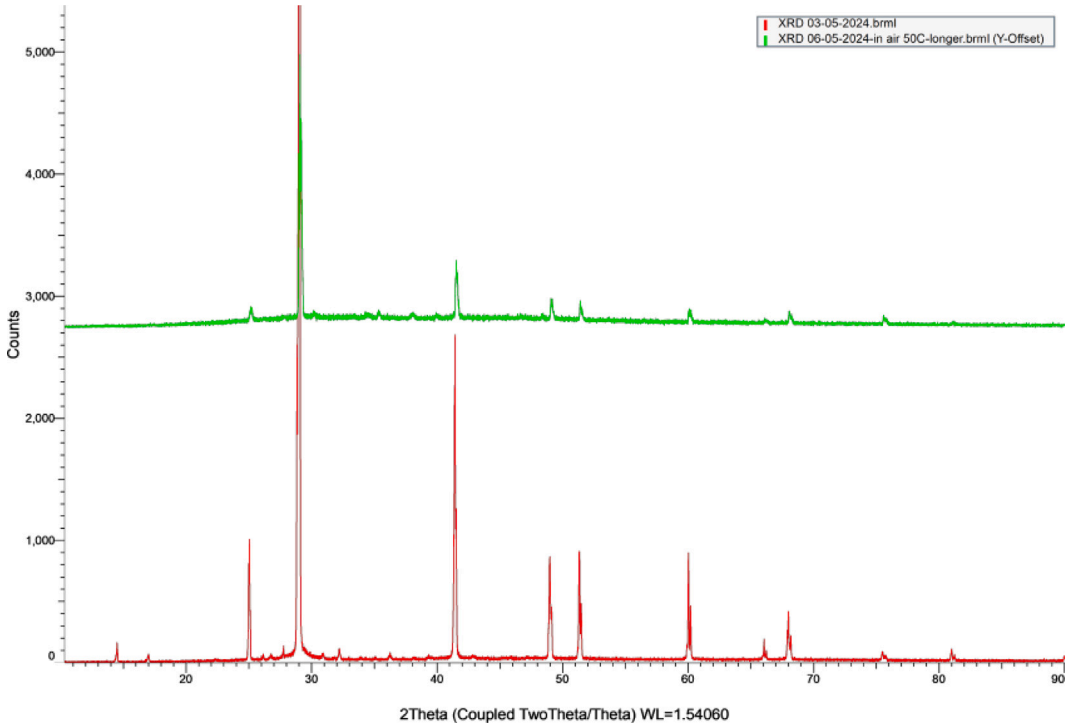

Fig. D.1. XRD measurements of $NaBH_4$ powder as received (red) and $NaBH_4$ powder which has absorbed water from ambient air (until it was completely dissolved) and subsequently dried at 50 °C (green). The *y*-axis offset of the latter is used purely to improve readability.

0.33 mm, D/d = 255 and W/d = 60.1, such that h/d is approximately 20 for 1 rpm. Félix et al. did not investigate rotational speeds of 60 rpm, but extrapolating their results for speeds up to 20 rpm, similar h/d values can be found as for 1 rpm.

Félix et al. also measured the velocity profiles for various rotational speeds across the flowing layer. Extrapolating their results, a conservative estimate of the average flow velocity would be 2 cm/s (1 rpm) and 120 cm/s (60 rpm), independent of the particle size.

Using this, we can estimate the inertial number for both granules and powder, for both rotational speeds, substituting θ with the corresponding dAoR. For 1 rpm:

$$I_{granules,1} = \frac{5}{2}\frac{0.02 \cdot 1.8 \cdot 10^{-3}}{5 \cdot 1.8 \cdot 10^{-3}\sqrt{9.81 \cdot 5 \cdot 1.8 \cdot 10^{-3} \cdot \cos(40°)}} \approx 3.8 \cdot 10^{-2}$$

$$I_{powder,1} = \frac{5}{2}\frac{0.02 \cdot 0.33 \cdot 10^{-3}}{20 \cdot 0.33 \cdot 10^{-3}\sqrt{9.81 \cdot 20 \cdot 0.33 \cdot 10^{-3} \cdot \cos(40°)}} \approx 1.1 \cdot 10^{-2}$$

For 60 rpm, we need to scale the found inertial numbers with the ratio of the average flow velocities, 1.2/0.02, such that:

$$I_{granules,60} = I_{granules,1}\frac{1.2}{0.02} \approx 2.28$$

$$I_{powder,60} = I_{powder,1}\frac{1.2}{0.02} \approx 0.66$$

Consequently, the flowing layer of both granules and powder can be classified as dense flowing, which transition into the gaseous flow regime for increasing the rotational speed to 60 rpm. It has to be noted that these are estimates, but since both $I_{granules,60}$ and $I_{powder,60}$ are significantly higher than the threshold for the gaseous regime (0.1–0.3), we can safely assume that the 60 rpm experiments approach this regime, at minimum.

Appendix B. Additional ring shear test results

See Figs. B.1–B.3.

Appendix C. Additional rotating drum results

See Figs. C.1 and C.2.

Appendix D. XRD measurements

See Fig. D.1.

Data availability

Raw data, processing scripts, and other supportive data is stored in a data repository [43].

References

[1] W. Ramsay, E. Fridell, M. Michan, Maritime energy transition: future fuels and future emissions, J. Mar. Sci. Appl. 22 (4) (2023) 681–692, http://dx.doi.org/10.1007/s11804-023-00369-z, ISSN: 1671-9433, 1993-5048.

[2] E. Rivard, M. Trudeau, K. Zaghib, Hydrogen storage for mobility: a review, Materials (ISSN: 1996-1944) 12 (12) (2019) 1973, http://dx.doi.org/10.3390/ma12121973.

[3] E.S. van Rheenen, J.T. Padding, C. Slootweg, K. Visser, A review of the potential of hydrogen carriers for zero emission, low signature ship propulsion systems, in: Conference Proceedings of INEC, 2022, http://dx.doi.org/10.24868/10649.

[4] D. Alligier, E. Petit, U.B. Demirci, A boron-11 NMR study of the stability of the alkaline aqueous solution of sodium borohydride that is both an indirect fuel and a direct fuel for low-temperature fuel cells, Int. J. Hydrog. Energy (ISSN: 03603199) 47 (55) (2022) 23310–23315, http://dx.doi.org/10.1016/j.ijhydene.2022.05.119.

[5] J. Ma, N.A. Choudhury, Y. Sahai, A comprehensive review of direct borohydride fuel cells, Renew. Sustain. Energy Rev. (ISSN: 1364-0321) 14 (1) (2010) 183–199, http://dx.doi.org/10.1016/j.rser.2009.08.002.

[6] N. Luo, G.H. Miley, K.J. Kim, R. Burton, X. Huang, NaBH4/H2O2 fuel cells for air independent power systems, J. Power Sources (ISSN: 03787753) 185 (2) (2008) 685–690, http://dx.doi.org/10.1016/j.jpowsour.2008.08.090.

[7] R.M. Mohring, R.E. Luzader, A sodium borohydride on-board hydrogen generator for powering fuel cell and internal combustion engine vehicles, 2001, pp. 2001–01–2529, http://dx.doi.org/10.4271/2001-01-2529.

[8] S. Kwon, M.J. Kim, S. Kang, T. Kim, Development of a high-storage-density hydrogen generator using solid-state NaBH4 as a hydrogen source for unmanned aerial vehicles, Appl. Energy (ISSN: 03062619) 251 (2019) 113331, http://dx.doi.org/10.1016/j.apenergy.2019.113331.

[9] P. Gislon, G. Monteleone, P. Prosini, Hydrogen production from solid sodium borohydride, Int. J. Hydrog. Energy (ISSN: 03603199) 34 (2) (2009) 929–937, http://dx.doi.org/10.1016/j.ijhydene.2008.09.105.

[10] W. Chen, L.Z. Ouyang, J.W. Liu, X.D. Yao, H. Wang, Z.W. Liu, M. Zhu, Hydrolysis and regeneration of sodium borohydride (NaBH4) – A combination of hydrogen production and storage, J. Power Sources (ISSN: 0378-7753) 359 (2017) 400–407, http://dx.doi.org/10.1016/j.jpowsour.2017.05.075.

[11] T. Kim, NaBH4 (sodium borohydride) hydrogen generator with a volume-exchange fuel tank for small unmanned aerial vehicles powered by a PEM (proton exchange membrane) fuel cell, Energy (ISSN: 03605442) 69 (2014) 721–727, http://dx.doi.org/10.1016/j.energy.2014.03.066.

[12] G.M. Arzac, A. Fernández, A. Justo, B. Sarmiento, M.A. Jiménez, M.M. Jiménez, Optimized hydrogen generation in a semicontinuous sodium borohydride hydrolysis reactor for a 60W-scale fuel cell stack, J. Power Sources (ISSN: 03787753) 196 (9) (2011) 4388–4395, http://dx.doi.org/10.1016/j.jpowsour.2010.10.073.

[13] M. Rivarolo, O. Improta, L. Magistri, M. Panizza, A. Barbucci, Thermo-economic analysis of a hydrogen production system by sodium borohydride (NaBH4), Int. J. Hydrog. Energy (ISSN: 0360-3199) 43 (3) (2018) 1606–1614, http://dx.doi.org/10.1016/j.ijhydene.2017.11.079.

[14] D.M.F. Santos, C.A.C. Sequeira, Sodium borohydride as a fuel for the future, Renew. Sustain. Energy Rev. (ISSN: 1364-0321) 15 (8) (2011) 3980–4001, http://dx.doi.org/10.1016/j.rser.2011.07.018.

[15] U.B. Demirci, The hydrogen cycle with the hydrolysis of sodium borohydride: A statistical approach for highlighting the scientific/technical issues to prioritize in the field, Int. J. Hydrog. Energy (ISSN: 0360-3199) 40 (6) (2015) 2673–2691, http://dx.doi.org/10.1016/j.ijhydene.2014.12.067.

[16] M.C. van Benten, J.T. Padding, D.L. Schott, Circular bunkering for maritime vessels using sodium borohydride, Renew. Sustain. Energy Rev. (ISSN: 1364-0321) 223 (2025) 116039, http://dx.doi.org/10.1016/j.rser.2025.116039.

[17] F. Da Cruz, S. Emam, M. Prochnow, J.-N. Roux, F. Chevoir, Rheophysics of dense granular materials: Discrete simulation of plane shear flows, Phys. Rev. E - Stat. Nonlinear, Soft Matter Phys. (ISSN: 1550-2376) 72 (2) (2005) http://dx.doi.org/10.1103/PhysRevE.72.021309.

[18] I. Iordanoff, M.M. Khonsari, Granular lubrication: toward an understanding of the transition between kinetic and quasi-fluid regime, J. Tribol. (ISSN: 0742-4787) 126 (1) (2004) 137–145, http://dx.doi.org/10.1115/1.1633575.

[19] O. Pouliquen, F. Chevoir, Dense flows of dry granular material, Comptes Rendus Phys. (ISSN: 16310705) 3 (2) (2002) 163–175, http://dx.doi.org/10.1016/S1631-0705(02)01309-9.

[20] G.D.R. Midi, On dense granular flows, Eur. Phys. J. E (ISSN: 1292-8941) 14 (4) (2004) 341–365, http://dx.doi.org/10.1140/epje/i2003-10153-0.

[21] T.M. Povall, I. Govender, A.T. McBride, Dense granular flows in rotating drums: A computational investigation of constitutive equations, Powder Technol. (ISSN: 0032-5910) 393 (2021) 238–249, http://dx.doi.org/10.1016/j.powtec.2021.07.051.

[22] I. Govender, Granular flows in rotating drums: A rheological perspective, Miner. Eng. (ISSN: 0892-6875) 92 (2016) 168–175, http://dx.doi.org/10.1016/j.mineng.2016.03.021.

[23] E. DeGiuli, G. Düring, E. Lerner, M. Wyart, Unified theory of inertial granular flows and non-Brownian suspensions, Phys. Rev. E 91 (6) (2015) 062206, http://dx.doi.org/10.1103/PhysRevE.91.062206, ISSN: 1539-3755, 1550-2376.

[24] E. DeGiuli, J.N. McElwaine, M. Wyart, Phase diagram for inertial granular flows, Phys. Rev. E 94 (1) (2016) 012904, http://dx.doi.org/10.1103/PhysRevE.94.012904, ISSN: 2470-0045, 2470-0053.

[25] Kahlil F.E. Cui, Gordon G.D. Zhou, Teng Man, Yu Huang, Yongshuang Zhang, Xueqiang Lu, Tao Zhao, Modeling the dense granular flow rheology of particles with different surface friction: implications for geophysical mass flows, J. Geophys. Res.: Earth Surf. 130 (3) (2025) e2024JF008048, http://dx.doi.org/10.1029/2024JF008048, ISSN: 2169-9003, 2169-9011.

[26] J. Krzyżanowski, J. Tejchman, W. Soł owski, M. Wójcik, Modelling of shear zones during quasi-static granular silo flow using material point method (MPM), Powder Technol. (ISSN: 0032-5910) 378 (2021) 538–560, http://dx.doi.org/10.1016/j.powtec.2020.10.001.

[27] P. Toson, J.G. Khinast, Impulse-based dynamics for studying quasi-static granular flows: Application to hopper emptying of non-spherical particles, Powder Technol. (ISSN: 0032-5910) 313 (2017) 353–360, http://dx.doi.org/10.1016/j.powtec.2017.03.016.

[28] H. Guo, X. Yang, Z. Tian, T. Li, X. Liu, DEM modeling of the dilute-to-dense transition of granular flow in silos, Powder Technol. (ISSN: 0032-5910) 436 (2024) 119472, http://dx.doi.org/10.1016/j.powtec.2024.119472.

[29] A. López, V. Vivacqua, R. Hammond, M. Ghadiri, Analysis of screw feeding of faceted particles by discrete element method, Powder Technol. (ISSN: 0032-5910) 367 (2020) 474–486, http://dx.doi.org/10.1016/j.powtec.2020.03.064.

[30] E. Rabinovich, H. Kalman, Flow regime diagram for vertical pneumatic conveying and fluidized bed systems, Powder Technol. (ISSN: 0032-5910) 207 (1) (2011) 119–133, http://dx.doi.org/10.1016/j.powtec.2010.10.017.

[31] A. Seiphoori, T.N.M. Duong, M. Geyin, A mechanistic understanding of interface shear behavior of cohesionless materials using torsional ring shear test, in: Proceedings of the 3rd Vietnam Symposium on Advances in Offshore Engineering, 2024.

[32] H. Louati, D. Oulahna, A. de Ryck, Effect of the particle size and the liquid content on the shear behaviour of wet granular material, Powder Technol. (ISSN: 0032-5910) 315 (2017) 398–409, http://dx.doi.org/10.1016/j.powtec.2017.04.030.

[33] J. Fitzpatrick, T. Iqbal, C. Delaney, T. Twomey, M.K Keogh, Effect of powder properties and storage conditions on the flowability of milk powders with different fat contents, J. Food Eng. (ISSN: 0260-8774) 64 (4) (2004) 435–444, http://dx.doi.org/10.1016/j.jfoodeng.2003.11.011.

[34] V. Garg, T. Deng, M.S.A. Bradley, A new method for assessing powder flowability based on physical properties and cohesiveness of particles using a small quantity of samples, Powder Technol. (ISSN: 0032-5910) 395 (2022) 708–719, http://dx.doi.org/10.1016/j.powtec.2021.10.027.

[35] A.M. Stoklosa, R.A. Lipasek, L.S. Taylor, L.J. Mauer, Effects of storage conditions, formulation, and particle size on moisture sorption and flowability of powders: A study of deliquescent ingredient blends, Food Res. Int. (ISSN: 0963-9969) 49 (2) (2012) 783–791, http://dx.doi.org/10.1016/j.foodres.2012.09.034.

[36] H. Kalman, Particle breakage and attrition, KONA Powder Part. J. 18 (2000) 108–120, http://dx.doi.org/10.14356/kona.2000017.

[37] H. Kalman, Effect of moisture content on flowability: Angle of repose, tilting angle, and Hausner ratio, Powder Technol. (ISSN: 00325910) 393 (2021) 582–596, http://dx.doi.org/10.1016/j.powtec.2021.08.010.

[38] E. Teunou, J. Fitzpatrick, Effect of storage time and consolidation on food powder flowability, J. Food Eng. (ISSN: 0260-8774) 43 (2) (2000) 97–101, http://dx.doi.org/10.1016/S0260-8774(99)00137-5.

[39] CPH Chemicals, URL https://www.cphchemicals.com/.

[40] M. Murtomaa, E. Laine, J. Salonen, O. Kuusinen, On effects of ambient humidity on sodium borohydride powder, Powder Handl. Process. 11 (1999).

[41] A.M. Beaird, T.A. Davis, M.A. Matthews, Deliquescence in the hydrolysis of sodium borohydride by water vapor, Ind. Eng. Chem. Res. (ISSN: 0888-5885) 49 (20) (2010) 9596–9599, http://dx.doi.org/10.1021/ie100244v.

[42] P. Li, L. Yu, M.A. Matthews, W.A. Saidi, J.K. Johnson, Deliquescence of NaBH4 from density functional theory and experiments, Ind. Eng. Chem. Res. (ISSN: 0888-5885) 52 (38) (2013) 13849–13861, http://dx.doi.org/10.1021/ie401742u.

[43] M.C. van Benten, J.T. Padding, D.L. Schott, Data and scripts underlying the publication: experimental characterisation of granular sodium borohydride under varying operational conditions across flow [dataset], 4TU.ResearchData, 2025, http://dx.doi.org/10.4121/d4e53185-56ef-4acf-8f71-cc34d46a8319.

[44] D. Schulze, Ring Shear Testers, https://www.dietmar-schulze.de/ringschergeraete_e.html.

[45] D. Schulze, Powders and Bulk Solids: Behavior, Characterization, Storage and Flow, Springer, ISBN: 978-3-540-73767-4, 2008.

[46] S.W. Lommen, D.L. Schott, G. Lodewijks, DEM speedup: stiffness effects on behavior of bulk material, Particuology (ISSN: 1674-2001) 12 (2014) 107–112, http://dx.doi.org/10.1016/j.partic.2013.03.006.

[47] T. Roessler, A. Katterfeld, Scaling of the angle of repose test and its influence on the calibration of DEM parameters using upscaled particles, Powder Technol. (ISSN: 0032-5910) 330 (2018) 58–66, http://dx.doi.org/10.1016/j.powtec.2018.01.044.

[48] S.M. Derakhshani, D.L. Schott, G. Lodewijks, Micro–macro properties of quartz sand: experimental investigation and DEM simulation, Powder Technol. (ISSN: 0032-5910) 269 (2015) 127–138, http://dx.doi.org/10.1016/j.powtec.2014.08.072.

[49] A. Neveu, F. Francqui, G. Lumay, Measuring powder flow properties in a rotating drum, Measurement (ISSN: 0263-2241) 200 (2022) 111548, http://dx.doi.org/10.1016/j.measurement.2022.111548.

[50] P.C. Van der Sande, Granular Flow in Stirred Bed Reactors, (Ph.D. thesis), 2025, http://dx.doi.org/10.4233/uuid:95db25ba-7936-497d-9106-7cc31285bb13.

[51] V.N. Tondare, J.G. Whiting, A.L. Pintar, S.P. Moylan, A. Neveu, F. Francqui, An interlaboratory study for assessing repeatability and reproducibility of the data generated by rotating drum powder rheometers (part 1: granudrum), Powder Technol. (ISSN: 0032-5910) 441 (2024) 119810, http://dx.doi.org/10.1016/j.powtec.2024.119810.

[52] J. Mellmann, The transverse motion of solids in rotating cylinders—Forms of motion and transition behavior, Powder Technol. (ISSN: 0032-5910) 118 (3) (2001) 251–270, http://dx.doi.org/10.1016/S0032-5910(00)00402-2.

[53] S. Pourandi, P.C. Van Der Sande, T. Weinhart, I. Ostanin, A mathematical model for the dynamic angle of repose of a granular material in the rotating drum, Powder Technol. (ISSN: 00325910) 446 (2024) 120176, http://dx.doi.org/10.1016/j.powtec.2024.120176.

[54] S.H. Larsson, Kinematic wall friction properties of reed canary grass powder at high and low normal stresses, Powder Technol. (ISSN: 0032-5910) 198 (1) (2010) 108–113, http://dx.doi.org/10.1016/j.powtec.2009.10.022.

[55] E. Xanthakis, R.J. Ommen, L. Ahrné, Flowability characterization of nanopowders, Powder Technol. (ISSN: 0032-5910) 286 (2015) 156–163, http://dx.doi.org/10.1016/j.powtec.2015.08.015.

[56] X. Yu, D. Wang, Z. Chen, S. He, H. Li, Y. Xu, Experimental investigation on rheological behavior of dry granular mixtures based on direct measurement of basal friction, Powder Technol. (ISSN: 00325910) 438 (2024) 119674, http://dx.doi.org/10.1016/j.powtec.2024.119674.

[57] J. Nie, S. Zhao, Y. Cui, Y. Wang, Coupled effects of particle overall regularity and sliding friction on the shear behavior of uniformly graded dense sands, J. Rock Mech. Geotech. Eng. (ISSN: 16747755) 14 (3) (2022) 873–885, http://dx.doi.org/10.1016/j.jrmge.2021.10.014.

[58] J.A. Prusiel, L. Andrzej, Investigation of heat and moisture effects in silos containing agricultural bulk solids, ResearchGate (2007) http://dx.doi.org/10.1002/ppsc.200701119.

[59] G. Félix, V. Falk, U. D'Ortona, Granular flows in a rotating drum: The scaling law between velocity and thickness of the flow, Eur. Phys. J. E 22 (1) (2007) 25–31, http://dx.doi.org/10.1140/epje/e2007-00002-5, ISSN: 1292-8941, 1292-895X.